Improving wave-based air-sea momentum flux parameterization in mixed seas

César Sauvage[1], Hyodae Seo[1], Carol Anne Clayson[1], and James B. Edson[1].

[1]Woods Hole Oceanographic Institution, Woods Hole, Massachusetts, USA

Key Points:

- Surface stress at moderate to high winds is dominated by short wind waves.
- COARE3.5 wave based formulation can underestimates surface stress by more than 10 % in mixed sea conditions under moderate to high wind.
- Using the mean wave period or including the directional alignment between wind and wave in COARE3.5 alleviates this issue.

Corresponding author: César Sauvage, `csauvage@whoi.edu`

Abstract

In winter, the Northwest Tropical Atlantic Ocean can be characterized by various wave age-based interactions among ocean current, surface wind and surface waves, which are critical for accurately describing surface wind stress. In this work, coupled wave-ocean-atmosphere model simulations are conducted using two different wave roughness parameterizations within COARE3.5, including one that relies solely on wind speed and another that uses wave age and wave slope as inputs. Comparisons with the directly measured momentum fluxes during the ATOMIC/EUREC^{4}A experiments in winter 2020 show that, for sea states dominated by short wind waves under moderate to strong winds, the wave-based formulation increases the surface roughness length in average by 25% compared to the wind-speed-based approach. For sea states dominated by remotely generated swells under moderate to strong wind intensity, the wave-based formulation predicts significantly lower roughness length and surface stress (≈15%), resulting in increased near-surface wind speed above the constant flux layer (≈5%). Further investigation of the mixed sea states in the model and data indicates that the impact of swell on wind stress is overemphasized in the COARE3.5 wave-based formulation, especially under moderate wind regimes. Various approaches are explored to alleviate this deficiency by either introducing directional alignment between wind and waves or using the mean wave period instead of the wave period corresponding to the spectral peak to compute the wave age. The findings of this study are likely to be site-dependent, and mostly concern specific regimes of wind and waves where the original parameterization was deficient.

Plain Language Summary

Accurately understanding and describing air-sea interactions is critical for weather forecast and regional climate. In this work, we use numerical experiments with and without taking into account the ocean waves to describe air-sea interactions. Most of the momentum exchange between the ocean and the atmosphere is done through locally wind-generated waves, however remotely generated waves, such as swells, can also interfere in these air-sea interactions. Comparisons with observations made during the ATOMIC/EUREC^{4}A field campaigns in winter 2020 show in particular that our numerical experiment overestimated the impact of the swell on the atmosphere. Various approaches are explored here to alleviate this deficiency, one of those being the introduction of the effect of the alignment between wind and waves.

1 Introduction

Over the ocean, most of the momentum, heat, and mass exchanges with the atmosphere are supported by short wind-waves on spatial scales of O(0.1-10m). These wind-waves enhance the surface drag and roughness at the air-sea interface, thereby increasing the wind stress. The wind stress is coupled with the planetary boundary layer (PBL) processes in the atmosphere, modifying the kinematic and thermodynamic profiles in this lowest part of the atmosphere (Janssen, 1989; Moon et al., 2004). In addition to locally generated wind-waves, the sea state is also influenced by the remotely generated swell, especially in the lower latitudes, whose propagation direction is often uncorrelated with local winds. The fast-propagating swell wave that is strongly misaligned with or outruns the local wind can be a conduit for upward momentum and energy transfer from waves to the wind, forming a wave-driven low-level jet (e.g., Harris, 1966; Sullivan et al., 2008; Hanley & Belcher, 2008) and dissipating the swell waves (M. Donelan, 1999; Kahma et al., 2016; Liu et al., 2017).

In numerical models, the wind stress over the oceans is parameterized using bulk flux algorithms, such as the Coupled Ocean-Atmosphere Response Experiment (COARE, Fairall et al., 1996, 2003; Edson et al., 2013). If no coincident wave fields are available, COARE parameterizes the wave roughness length (z_0) using wind speeds only. In this study, this approach will be referred to as the wind-speed-dependent formulation (WSDF). Since wind and wind-waves are in near-equilibrium in many cases over the extratropical open oceans, the COARE's WSDF tends to accurately predict the surface roughness and thereby the surface stress (Edson et al., 2013). However, under trade-wind regimes in the tropics such as our study region in boreal winter, remotely-generated swell significantly shape the sea state, whose effect on wind stress cannot be accurately characterized by local wind alone. To improve estimates of the fluxes under these conditions, "wave-based" formulations exist in many bulk flux algorithms that model z_0 as a function of wave age or wave age/slope (e.g,. Taylor & Yelland, 2001; Oost et al., 2002; Drennan et al., 2003; Edson et al., 2013; Sauvage et al., 2020). As there are increasing interests and opportunities to incorporate the wave effects on surface fluxes in numerical models, such wave-based formulations (WBF) in bulk formulas will likely be adopted more in such models. Since the parameterized surface fluxes serve as lower boundary conditions for turbulent exchanges within the atmospheric and oceanic boundary layers, the simulation and forecast skills will be influenced by the physics and assumptions represented in the bulk formulas. Therefore, it is imperative to understand the assumptions and deficiencies in current WBFs and offer possible revisions to the formulations for air-sea fluxes with increased accuracy. The goal of this paper is to enhance a regime-based understanding of wave-wind interactions via detailed validation of the parameterized air-sea flux from high-resolution coupled model simulations against directly measured air-sea fluxes.

This study focuses on air-sea momentum flux during the ATOMIC/EUREC^{4}A field campaign. The ATOMIC (Atlantic Tradewind Ocean-Atmosphere Mesoscale Interaction Campaign) is the U.S. complement to the European field campaign, EUREC^{4}A (ElUcidating the RolE of Cloud–Circulation Coupling in ClimAte, Stevens et al., 2021), both of which took place in the Northwest Tropical Atlantic Ocean in January-February 2020 (Figure 1). The primary objective of this study is to determine how well the current WBF in an advanced bulk flux algorithm such as COARE3.5 reproduces the observed wind stress in the mixed sea conditions compared to the WSDF. By exploiting the fully-coupled ocean-atmosphere-wave model simulations and extensive analyses of the in situ observational datasets, we will attempt to explain the causes for discrepancies between simulated and measured wind stresses. Our results indicate that the current COARE3.5 WBF underestimates z_0 and wind stress, particularly over the mixed sea state. We will show that this is due to either a missing physics of the wave-wind interaction or using an inappropriate wave input parameter to describe the mixed sea condition.

The paper is organized as follows. Section 2.1 describes the technical details of the latest z_0 formulation in COARE3.5. Sections 2.2 and 2.3 discuss the fully coupled ocean-atmosphere-wave modeling system used in the investigation, followed by the details on the experimental design and observational datasets in Section 2.4 and Section 2.5, respectively. The wave impact on z_0, wind stress, and low-level winds are discussed in a case study investigation in Section 3. Section 4 provides an in-depth comparison of the parameterized momentum flux against the direct measurements, identifying the areas and regimes for further improvement. In section 5, possible approaches are proposed and tested to alleviate the biases. Section 6 provides a summary and discussion.

2 Air-sea flux parameterization and coupled model

This section provides a brief overview of the wave-mediated momentum flux implemented in the Coupled Ocean-Atmosphere Response Experiment parameterization (COARE3.5, Fairall et al., 1996, 2003; Edson et al., 2013). Hereafter, we will focus on the COARE3.5 version, although a slightly updated version, COARE3.6, has been made publicly available. However, the findings of this study would stay unchanged when using COARE3.6 (not shown).

2.1 Roughness length and momentum flux in COARE3.5

The along wind stress in the COARE framework is defined as:

$$\tau = \rho C_D(z, z_0, \psi_m) U_r(z) S_r(z) = \rho u_*^2, \tag{1}$$

where ρ_a is the air density, $U_r(z)$ is the magnitude of the along-wind component of the wind vector, $S_r(z)$ is the scalar wind speed, where the subscript r denotes relative to the ocean surface; and u_* the friction velocity. C_D is the drag coefficient defined as:

$$C_D(z, z_0, \psi_m) = \left[\frac{\kappa}{ln(z/z_0) - \psi_m(\zeta)}\right]^2, \tag{2}$$

where κ is the von Kármán constant, $\psi_m(\zeta)$ is an empirical function of atmospheric stability, ζ is the z/L ratio with L the Obukhov length and z the height above the surface (Fairall et al., 1996). The surface roughness length z_0 is parameterized in COARE3.5 as the sum of two terms:

$$z_0 = z_0^{smooth} + z_0^{rough}, \tag{3}$$

where z_0^{smooth} and z_0^{rough} represent the smooth and rough flow components of z_0, respectively (Edson et al., 2013). The smooth flow component is parameterized as

$$z_0^{smooth} = \gamma \frac{\nu}{u_*}, \tag{4}$$

where γ is the roughness Reynolds number for smooth flow, set to be constant at 0.11 based on laboratory experiments, and ν is the kinematic viscosity. For smooth flow, the wind stress is mainly supported by viscous stress where $z_0 \approx z_0^{smooth}$.

The rough part of the roughness length, z_0^{rough}, is meant to parameterize the wind-driven gravity waves that support most of the stress above approximately 5 ms^{-1} when the sea becomes aerodynamically rough. This component of the roughness is formulated currently in several ways in COARE3.5. The simplest and the most broadly used way is to parameterize it as a function of wind speed only. The so-called wind speed dependent formulation without explicit wave and sea states inputs estimates z_0^{rough} using the Charnock's relation (Charnock, 1955):

$$z_0^{rough} = \frac{\alpha_{ch} u_*^2}{g}, \tag{5}$$

where g is the acceleration of gravity and α_{CH} is the Charnock coefficient that is dependent only on wind speed. COARE3.5 formulates α_{CH} as

$$\alpha_{ch} = mU_{r10N} + b, \tag{6}$$

where U_{r10N} is the 10-m wind speed relative to the sea surface under neutral conditions (Edson et al., 2013, Appendix) and coefficients m = 0.0017 and b = -0.005 (?, ?). Hereafter, U_{r10N} is defined such as:

$$U_{r10N} = \frac{u_*}{\kappa} ln(10/z_0), \tag{7}$$

The coefficients m, and b in Eq. 6, have been determined to fit the average data used in COARE3.5 over wind speeds between 5 and 18 ms^{-1}. If wind speed is below 5 ms^{-1}, the surface roughness is mainly determined by z_{smooth} in Eq. 4. For wind speeds greater than 18 ms^{-1}, COARE3.5 fixes the value of the Charnock coefficient to its value at 18 ms^{-1}. Note, however, that although α_{CH} is fixed above 18 ms^{-1}, z_0^{rough}, C_D and τ all continue to increase with the wind speed, just at a lower rate.

An alternative way to define z_0^{rough} in COARE3.5 is to use the so-called wave-based formulation (WBF), which requires contemporary information about the wave field and its state of development, such as significant wave height (H_s) and phase speed of the waves at the peak of the spectrum (c_p). Two WBFs are currently available in COARE3.5, one that uses the wave age only and another that uses both the wave age and wave steepness. In the second form, which is explored in this study in great detail, z_0^{rough} is expressed as

$$z_0^{rough} = H_s D(\frac{u_*}{c_p})^B, \tag{8}$$

where u_*/c_p is the inverse wave age based on the friction velocity, and D and B are numerical constants given by $D = 0.09$ and $B = 2$ in Edson et al. (2013). Hereafter, we will use a definition of wave age based on the ratio of the phase speed of the waves at the spectral peak over the surface wind speed at 10 m defined as

$$\chi = \frac{c_p}{U_{10}}. \tag{9}$$

The wave age is used to describe the state of development of the wave field. For example, a wave age close to 1.2 represents a fully developed sea when the surface waves and stress are largely in equilibrium (e.g., Phillips, 1985), in which the rate that wind does work on the surface waves is balanced by the dissipation rate of breaking waves (microbreakers and whitecaps) and nonlinear wave-wave interactions (e.g., Csanady & Gibson, 2001). Wave ages under 1 are associated with developing seas and young waves, while wave ages well above 1.2 describe decaying seas and swell. It should be noted that in the current COARE3.5, c_p is defined using the peak period of the waves, T_p, in deep water such that:

$$c_p = g\frac{T_p}{2\pi}. \tag{10}$$

In Section 3, we will examine the sensitivity of the estimated momentum flux based on the current COARE3.5 algorithm. Guided by comparison to the observations in Section 4, we will then explore the impacts of revised COARE3.5 WBF in Section 5.

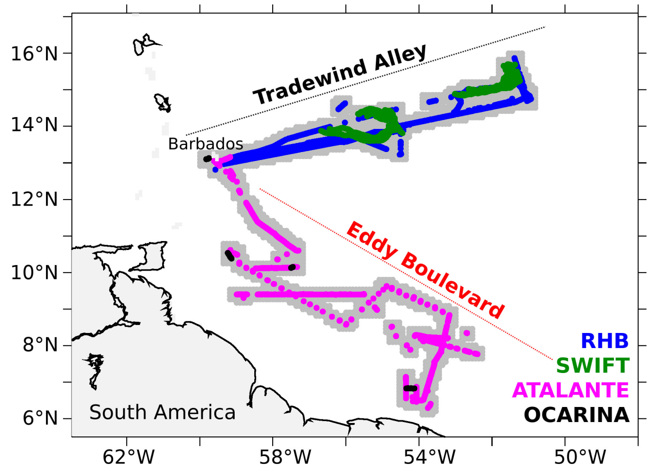

Figure 1. Tracks of the different platforms measuring surface stress. The gray area denotes where the model outputs are sampled along the tracks of observations. RHB provided data from January 9 to February 13, 2020. SWIFT drifters were deployed from 14 January to 22 January 2020 and from 30 January to 11 February 2020. R/V ATALANTE provided data from January 19 to February 19, 2020 and Ocarina was deployed periodically from January 25 to February 17, 2020.

2.2 SCOAR regional coupled model system

We use the Scripps Coupled Ocean-Atmosphere Regional (SCOAR) model (Seo et al., 2007, 2021), which couples the Weather Research and Forecast (WRF, Skamarock et al., 2008) Model to the Regional Ocean Modeling System (ROMS, Shchepetkin & McWilliams, 2005) via the COARE3.5 bulk flux algorithm (Fairall et al., 1996, 2003; Edson et al., 2013). In the absence of wave coupling, ROMS is driven by the surface heat flux (Q_{NET}), momentum flux (τ), and freshwater flux (Q_{FW}) computed from the wind speed-only formulation in COARE3.5 implemented in WRF. In turn, ROMS inputs SST and surface current vectors (U_s) to the COARE3.5 to compute the surface fluxes (Figure 2).

2.3 Wave coupling in SCOAR

This study implemented the coupling of the third-generation spectral wave model WaveWatch-III (WW3 Tolman et al., 2002; The WAVEWATCH III Development Group, 2016) into the SCOAR. Currently, two different ways are implemented to allow coupling waves to the atmosphere. The first option described in Figure 2 is based on the total friction velocity output from WW3 and used to estimate the wind stress and the resulting surface roughness length for computing turbulent heat fluxes. This option won't be used in this study. The second and third options described in Figure 2 are the focus of this manuscript and respectively take advantage of the COARE's WBF from (Edson et al., 2013), and the finding of this study. In this configuration, the centerpiece of the model coupling is the COARE3.5 implemented in the surface layer scheme in WRF to compute the air-sea fluxes. In this study, we use the Mellor-Yamada-Nakanishi-Niino (MYNN) surface layer scheme (Nakanishi & Niino, 2009; Jiménez et al., 2012), which over the ocean grid points computes the surface fluxes using the COARE3.5 WBF. WW3 is forced by the surface wind (U_{10}) from WRF and ocean current (U_s) from ROMS. WW3 then returns the significant wave height (H_s) and the phase speed of the dominant waves (c_p)

determined based on T_p (Eq. 10) to the MYNN surface layer scheme. In lieu of c_p, WW3 can alternatively send the mean phase speed (c_m) and peak wave direction (Section 5). Spatially varying Charnock coefficients (α_{CH}) are then updated to parameterize the surface roughness length (z_0) as a function of dominant wave age (χ) and wave steepness (Eq. 8). For this to work in WRF, the MYNN surface layer scheme has been modified to allow ingestion of wave age and significant wave height (H_s) from WW3. The MYNN PBL scheme (Nakanishi & Niino, 2004, 2006) is coupled to this modified surface layer scheme, allowing for the adjusted z_0, wind stress (τ), and latent (Q_{LH}) and sensible (Q_{SH}) heat fluxes to influence the kinematic and thermodynamics processes in the PBL. The surface layer scheme has also been modified to take the ocean surface currents (U_s) from ROMS to compute the relative wind and thus represent wind-current interaction. This so-called relative wind effect is represented in all simulations analyzed here. Wave to ocean coupling is also made available and ROMS can be forced by wave fields such as H_s and wave energy (FOC) fields. Wave-supported stress (τ^w) and wave dissipation (τ^{ds}) terms can also be send to ROMS to compute the ocean-side stress (τ^{oc}). For the purpose of this study, wave to ocean coupling is not included and thus on Figure 2 it is assumed that $\tau^{oc} = \tau^a$, where τ^a is the air-side stress.

2.4 Experiments

In WRF, the deep cumulus convection is represented through the Multi-scale Kain-Fritsch scheme (Zheng et al., 2016), the cloud micro-physics by the WRF single-moment 6-class scheme (Hong & Lim, 2006). The Goddard radiation scheme (Chou & Suarez, 1999) is used for shortwave and longwave radiation. The land surface process is treated with the Noah land surface model (F. Chen & Dudhia, 2001). In ROMS, the KPP (K profile parameterization) scheme (Large et al., 1994) determines vertical eddy viscosity and diffusivity. The vertical grid in ROMS is stretched to enhance the resolutions near the surface and the bottom, using the so-called stretching parameters of $\theta_s = 7.0$, $\theta_b = 2.0$, and h_{cline}= 300 m. In WW3, the set of parameterizations from Ardhuin et al. (2010) is used, including swell dissipation scheme (Ardhuin et al., 2009). Nonlinear wave–wave interactions are computed using the discrete interaction approximation (Hasselmann et al., 1985). Reflection by shorelines are enabled through Ardhuin and Roland (2012) scheme. The depth-induced breaking is based on Battjes and Janssen (1978), and the bottom friction formulation follows Ardhuin et al. (2003).

The model domain covers the Northwest Tropical Atlantic Ocean (Figure 3). The horizontal resolutions in WRF, ROMS, and WW3 are identical 10 km, with matching grids and land-sea masks. This horizontal resolution allows us to have reasonable description of the mixed sea state influenced by the remotely-generated swell and trade winds in the open oceans, which is the focus of this work. However, much finer-scale wind-wave and wave-current interactions, as studied in (Ardhuin et al., 2017; Bôas et al., 2020; Iyer et al., 2022), are not likely captured at this resolution, especially in the regions of strong currents and eddy variability. ROMS (WRF) is run with a stretched vertical grid with a total of 30 (33) vertical levels, with approximately 10 layers in the upper 150 m (below 1300 m). The model coupling is activated every 3 hours to account for the diurnal cycle.

A set of coupled model simulations presented in Section 4 is run for 6 months (November 1, 2019 to May 1, 2020), covering the ATOMIC/EUREC^{4}A period, with a specific aim to compare with the measurements. In these simulations, the WRF model is initialized and driven by 3-hourly ERA5 global reanalysis at 0.25° resolution (Hersbach et al., 2018a, 2018b), ROMS by the daily MERCATOR International global reanalysis at 1/12° resolution (Lellouche et al., 2018), and WW3 by seven spectral points obtained from the global 1/2° resolution WW3 simulations (Rascle

& Ardhuin, 2013). The initial conditions for ROMS and WW3 were obtained from the respective ROMS-only and WW3-only spin-up simulations forced by ERA5 atmospheric forcing (starting from January 1, 2019). In ROMS, the tidal forcing is obtained using the Oregon State University Tidal Prediction Software (Egbert & Erofeeva, 2002) and applied as a 2-D open boundary condition by prescribing the tidal period, elevation amplitude, current phase angle, current inclination angle, the minimum and maximum tidal current, and ellipse semi-minor axes for 13 major tidal constituents. Daily climatology estimates of the Amazon and River and Orinoco River discharges are obtained from the Observatory Service SO-HyBAM database (https://hybam.obs-mip.fr/), which are prescribed as point sources close to the river mouths in our grid.

The second set of simulations presented in Section 3 is identical to that of the 6-month-long simulations, except that WRF, ROMS, and WW3 are initialized from respectively 3-hourly ERA5 global reanalysis for the atmosphere and ROMS-only and WW3-only spin-up simulations for the ocean and waves as described above and run on a particular day (January 8, 2020) as a case study investigation. The motivation for the short simulations with the identical initial condition is to isolate the immediate impacts on z_0 and τ before the coupled feedback begins to alter the state variables. One could use the identical input state variables to estimate the air-sea fluxes offline using different COARE formulations. This yields similar results (not shown), indicating that the difference we show in Section 3 is not due to the difference in state variables, but due to the formulation difference. One notable advantage to use the fully coupled model simulation is that it allows for evaluating the wind response beyond the surface layer (e.g., Figure 6c), and potentially large-scale feedback effects via the coupling.

Table 1. Summary of the different SCOAR experiments.

Experiments	z_0 parameterization	Relative wind	Wave period	misaligned wave
WSDF	wind speed [Eq. 5]	yes	/	/
WBF	wave age + wave steepness [Eq. 8]	yes	T_p	no
WBF_θ	wave age + wave steepness [Eq. 11]	yes	T_p	yes
WBF_T_m	wave age + wave steepness [Eq. 12]	yes	T_m	no

Table 1 summarizes 4 experiments conducted in this study, where the only difference is in the way z_0 is parameterized in COARE3.5. In the first run (dubbed WSDF), the wind speed only formulation is used (hence, only WRF-ROMS coupling), while in the second run (WBF), the default wave-based formulation is used (WRF-ROMS-WW3). These two runs are examined in detail in Sections 3-4. Two additional runs, discussed in Section 5, are conducted with a modified wave-based formulation. WBF_θ takes into account the directional misalignment between wind and wave, while WBF_T_m modifies the definition of wave age based on mean wave period rather than the peak wave period.

All simulations used in this study produce output every 3h. Since this output interval is much coarser than the typical sampling intervals used in the observations (Section 2e), there is inevitable inconsistency in sampling frequency and the number of samples between the model and data. We attempt to increase the model sample size and capture more spatio-temporal variability by sampling a slightly broader region of the model domain encompassing the particular observational tracks (gray areas in Figure 1a). By doing this we assume that the spatial variability sampled in

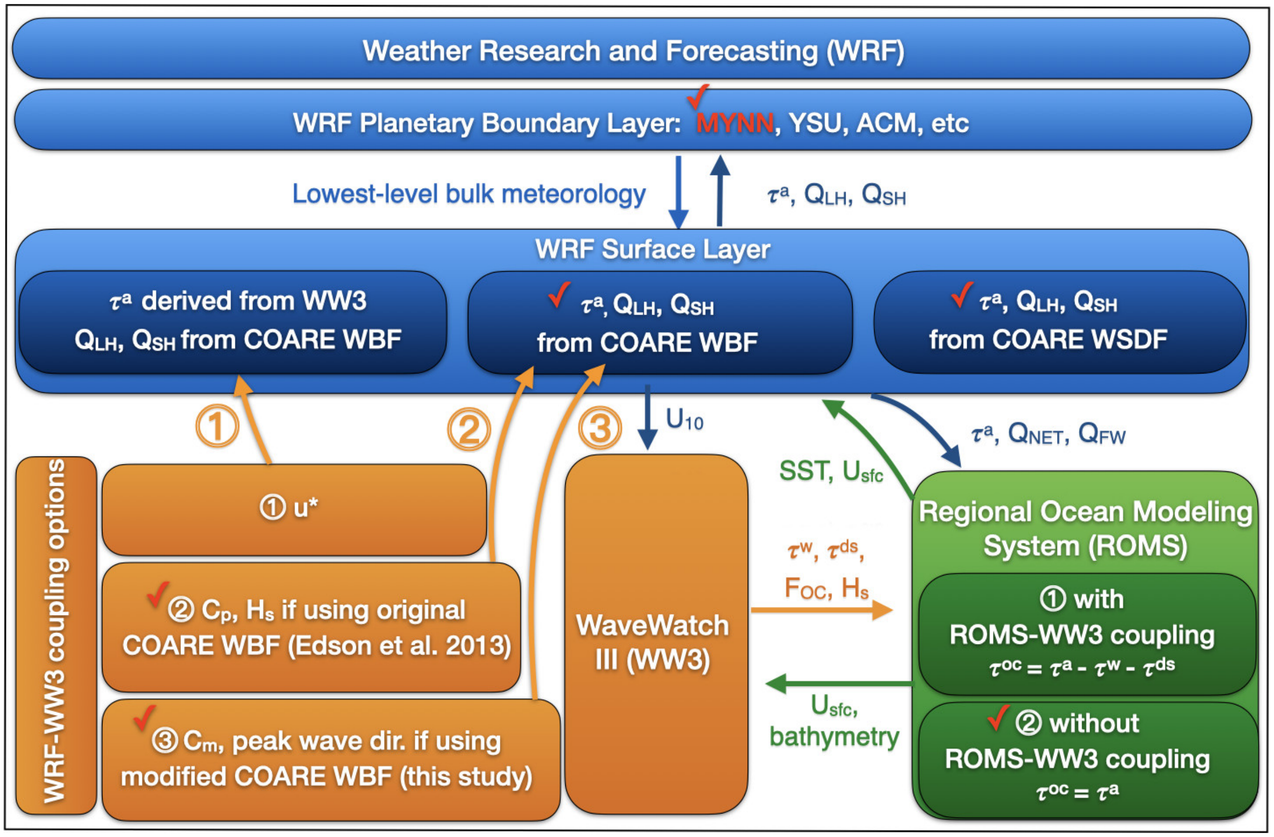

Figure 2. SCOAR WRF-ROMS-WW3 coupling flowchart. See the text for the variable names that are exchanged across the model components. Red ticks denote of the specific schemes and coupling methodology used in this study.

the model would resemble the temporal variability observed, considering that the spatial extent of our model sampling is still relatively close to the different platform tracks.

2.5 ATOMIC/EUREC^{4}A observations

This study will exploit direct and indirect measurements of momentum fluxes and relevant wave fields (i.e., significant wave height and wave period) from various platforms deployed during the ATOMIC/EUREC^{4}A experiment, summarized in Table 2. Figure 1 shows the tracks of the different observational platforms, including the NOAA R/V Ronald H. Brown (RHB, Quinn et al., 2021; Thompson et al., 2021), R/V ATALANTE (Bourras, Geyskens, et al., 2020), SWIFT drifters (Surface Wave Instrument Float with Tracking, Thomson, 2012; Thomson et al., 2019, 2021), and OCARINA (Ocean Coupled to Atmosphere, Research at the Interface with a Novel Autonomous platform, (Bourras, Branger, et al., 2020)) surface naval drone. The RHB provides direct momentum flux measurements every 10 minutes, using the eddy covariance method, in the so-called "Tradewind Alley" region from January 9 to February 13, 2020. The SWIFT drifters were deployed from the RHB, from which the hourly stress can be estimated using the equilibrium frequency range in the wave spectrum. More specifically, the directional wave spectra and bulk wave parameters were estimated from inertial motion observations. Then, the friction velocity at equilibrium u_* is calculated from the wave spectra, assuming a constant equilibrium frequency range over which the source and sink of wave energy is balanced (Iyer et al., 2022). They were deployed from 14 January to 22 January 2020 and from 30 January to 11 February 2020. The R/V ATALANTE measured the wind stress mostly in the "Eddy Boulevard" region based on the inertial dissipation method during the period of January 19 to February 19, 2020. OCARINA was deployed periodically from the R/V ATALANTE from January 25 to February 17, 2020, providing direct wind stress measurements every minute through the eddy covariance method.

Table 2. Summary of the different ATOMIC/EUREC^{4}A observations used in this study.

Platforms	R/V Ronald H. Brown	SWIFT	R/V ATALANTE	OCARINA
Observations	wind stress wave periods significant wave height	wind stress wave periods significant wave height	wind stress	wind stress
Methods used in estimating wind stress	eddy covariance	estimated through wave equilibrium subrange	inertial dissipation	eddy covariance
Periods	January 9 to February 13, 2020	14 January to 22 January 2020	January 19 to February 19, 2020	January 25 to February 17, 2020 (periodically)

RHB provided data from January 9 to February 13, 2020. SWIFT drifters were deployed from 14 January to 22 January 2020 and from 30 January to 11 February 2020. R/V ATALANTE provided data from January 19 to February 19, 2020 and Ocarina was deployed periodically from January 25 to February 17, 2020

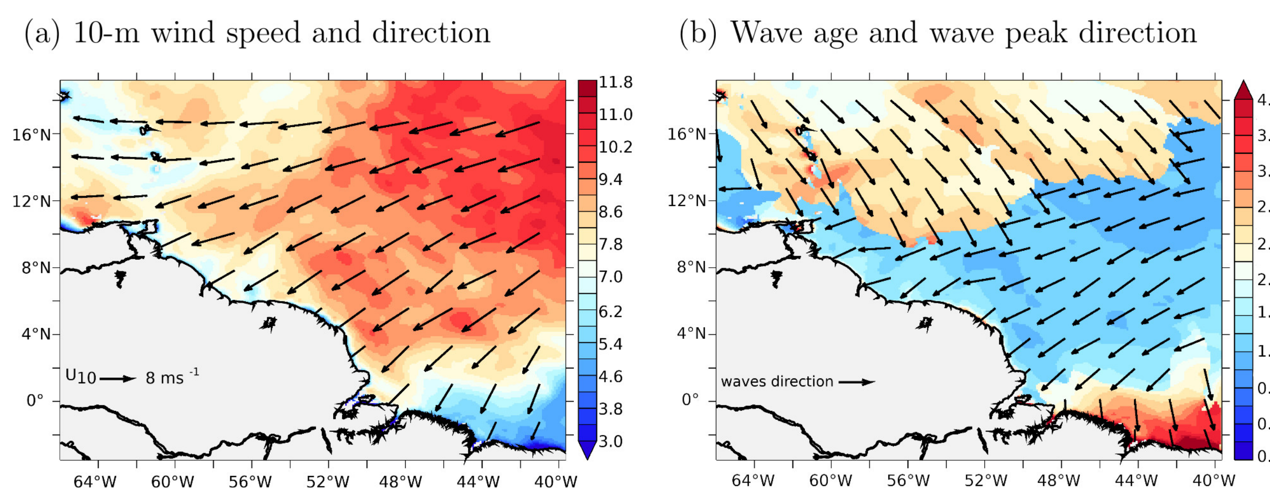

Figure 3. Snapshots of (a) 10-m wind speeds (shading, ms^{-1}) and direction (arrows) and (b) peak wave age (shading) and wave peak direction (arrows) on January 8, 2020 at 0600 UTC.

3 Impacts of wave and sea state: a case study

To demonstrate the immediate effect of including waves on z_0 and τ in the COARE3.5 using a coupled model, we will first compare the simulation results close to the initial condition. By doing so, the input state variables into the bulk formula remain largely identical, and any differences in simulated z_0 and τ can be attributed to the difference in the formulations. From this set of experiments, we will compare the results 3 hours after the initial condition.

The sea state and wind fields on January 8, 2020 at 0600 UTC, shown in Figure 3a, illustrate the archetypal synoptic condition observed in this region during the boreal winter. Much of the domain was under the influence of northeasterly trade winds with wind speeds of 7-13 ms^{-1}, while the northern and southeastern parts of the domain experienced much weaker (<7 ms^{-1}) easterly and northerly winds, respectively. Figure 3b shows the corresponding wave age and peak wave direction. In the Tradewind Alley region, surface waves were predominantly downwind with relatively small wave age, indicating the developing seas with young waves. Away from the trade winds, especially in the northern part of the domain, the wave vectors are generally misaligned with the local wind vectors, and the wave age is high, indicative of the swell-dominated sea state.

To illustrate sea state distribution differently, Figure 4a shows the probability density function (PDF) of wave age for the same period. Two distinct peaks of wave age stand out clearly. The first peak resides on wave age between 0.8 and 1.7, corresponding to developing (young) waves to fully developed (mature) seas. The secondary peak is found over a wide range of wave age greater than 1.7, reaching up to 4-5, the latter representing swell. Indeed, the fact that there is a gap at 1.7 strongly suggests that the older waves are swell, as opposed to the continuum of longer/older wind waves. Thus, in this case, we choose to use 1.7 as a threshold for fully developed seas and not the usual value of 1.2 which is what you might expect for wind waves dominated region. As a matter of fact, this swell-dominated sea state is frequently observed in the ATOMIC region in the boreal winter (e.g., Semedo et al., 2011; Jiang & Chen, 2013). Indeed, if considering the entire month of January 2020 in our simulations, we find that wave ages greater than 2 occur more than 60% of the time in this domain.

Figure 4b compares the z_0 against wind speed from the WSDF (black) and WBF (color) runs for this period. z_0 from WBF is color-coded to denote the corresponding wave age. The bottom panel shows stacked PDFs of 10-m wind speeds from WBF, with the red (gray) parts representing the proportion of wind associated with wage age over (under) 1.7. The WSDF in COARE3.5 assumes young seas under moderate to high winds, and hence the parameterized z_0 (black) obeys the well-known quadratic dependence on wind speed. The surface roughness z_0 from WSDF shows less scatter because it is based solely on wind speed.

In contrast, WBF captures the two wave age-dependent regimes of z_0 that appear distinct from WSDF. The first is the cluster of z_0, which increases more rapidly with wind speed than WSDF z_0 and occurs over 4-12 ms^{-1}. The wave age of this cluster (shading) is typically less than 1.7, corresponding to the first wave age peak in Figure 4a of small-scale young waves. Thus, the developing and equilibrium waves under these wind speeds and wave age conditions increase z_0 in WBF compared to WSDF.

The second cluster indicates significantly decreased z_0 in WBF with wind speed up to 12 ms^{-1}. This cluster can be further split into two different wind speed groups, under and above 8 ms^{-1}, color-coded by the PDF of winds (Figure 4b). Below 8 ms^{-1} (red, weak winds), the wave age mainly constitutes the tail of the

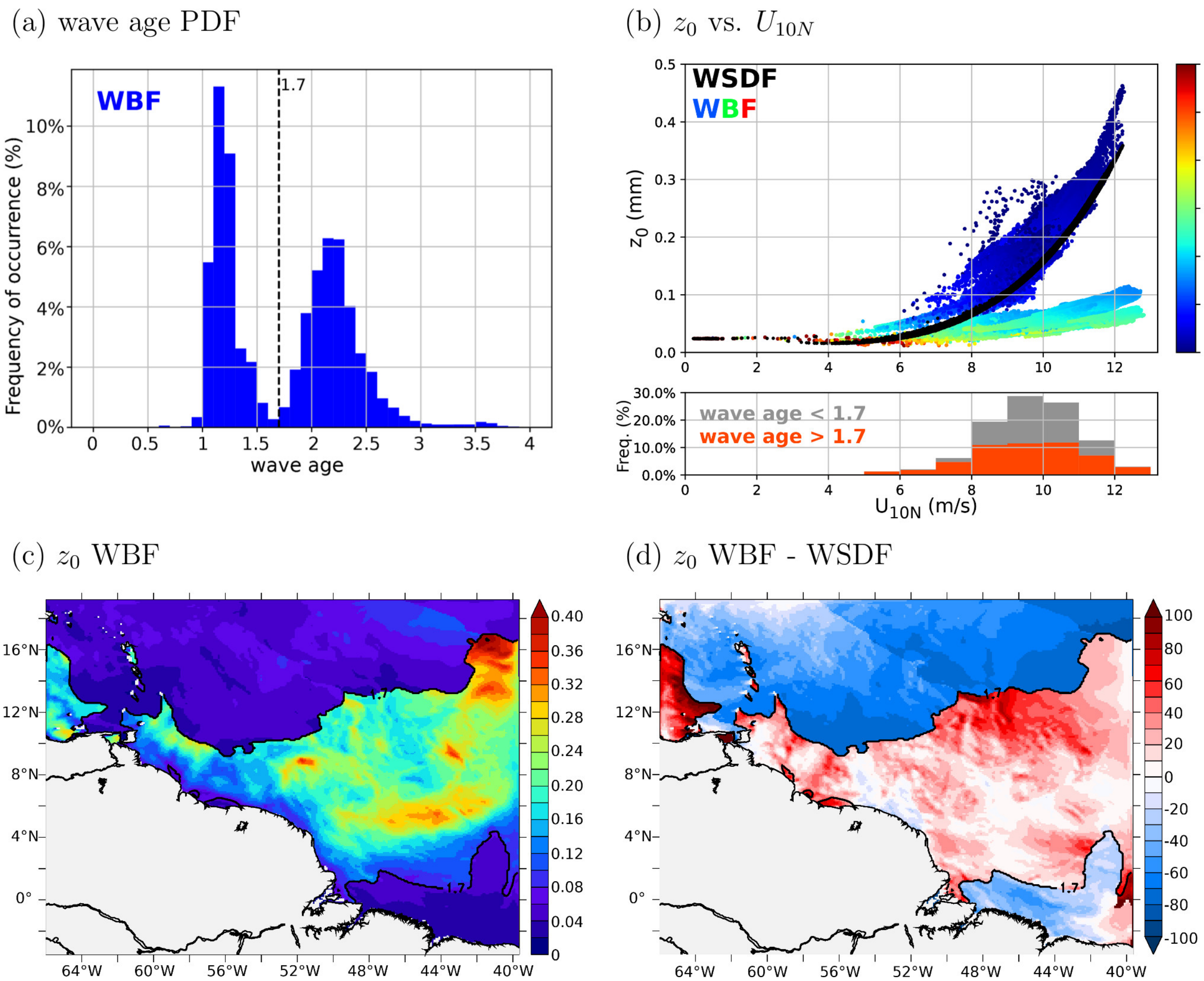

Figure 4. (a) PDF of wave age from the entire model domain on January 8, 2020 at 0600 UTC. The dotted vertical line denotes the wave age of 1.7, below (above) which the sea state is characterized as developing, equilibrium and slightly old waves (mature waves and swell). The upper panel of (b) is a scatter plot of z_0 (mm) vs. U_{10N} (ms^{-1}). z_0 from WSDF is shown in black, while z_0 from WBF is color-coded to denote the corresponding wave age. The stacked PDFs of U_{10N} in the lower panel of (b) are constructed when wave age is above 1.7 (red) and below 1.7 (gray). (c) A map of z_0 from WBF, superposed with a contour of wave age = 1.7. (d) A map of percentage difference of z_0 between WBF and WSDF

PDF distribution shown in Figure 4a with an average wave age of 2.7. It is where remotely generated swell appears to dominate the sea state. However, the wind speeds under 8 ms^{-1} account for less than 10% of the total wind speed data, and thereby it has a relatively small impact on the space/time-averaged z_0. Indeed, when averaged for wind speed below 8 ms^{-1}, the percentage difference in z_0 between WSDF and WBF, defined as (WBF-WSDF/WSDF)* 100, is only -1.7%.

During this day, most of the wind speed is above 8 ms^{-1}. In addition to the proportion of low wave age expected under this moderately high wind speed, we also find an increased occurrence of large wave age, accounting for 44% of the data (Figure 4b). The co-existence of high wind and swell indicates a mixed sea condition. In this case, when averaged over wind speed above 8 ms^{-1}, the swell impact appears much more significant, with z_0 in WBF being 15.7% lower than that in WSDF. The working hypothesis is that the use of the phase speed at the spectral peak causes the WBF to assume that the swell is supporting most of the stress even under moderate winds. This strong impact of swell on z_0 at such moderately strong winds is questionable, in the sense that the majority of air-sea momentum exchanges should still be supported by short-scale coupled wind waves despite the co-existence with the long-wave swell.

The spatial distribution of z_0 from WBF is shown in Figure 4c. The z_0 difference between WBF and WSDF is shown in Figure 4d. As in Figure 4a,b, two distinct regimes of z_0 are readily apparent on the map, delineated sharply by the contour of wave age 1.7 (black). The horizontal discontinuities in the wave and z_0 fields (Figure 4c,d) appear only with the use of the peak period, while the use of average wave period produces much smoother fields (not shown). The location of the front is only because this is a snapshot of the sea state on 8 January at 0600 UTC. Snapshots 3h before/after would show the swell front displaced to another location as the swell is moving/dissipating. In the first regime of increased z_0 in WBF under moderate to strong trade winds, the WBF predicts an increased z_0 by on average 25% compared to WSDF. This increased z_0 is expected as the WBF z_0 formulation (Eq. 8) takes into account the effect of wave slope on the aerodynamic roughness of the sea surface. That is, Figure 5a,b show that wave slope under young waves is higher, where the choppy sea surface increases z_0. Figure 5c,d shows the angle (θ) between the wind direction and peak wave direction. If $\theta = 0°$, wind and waves are perfectly aligned, whereas $\theta = 180°$ means wind and waves are opposed. Collocated with the regime of increased z_0, the peak wave direction is largely downwind, since θ is generally less than 50°. This corroborates that these waves are young waves driven by local winds. In the present study only the peak wave direction is used to defined alignment/misalignment with the local wind. However, at times, the wave field can yield significant directional spreading, this aspect is discussed later on in Section 5.2.

Figure 4d also shows the second regime of decreased z_0 with the inclusion of waves, especially in the northern part of the domain. In this region, the remotely generated swell propagates into the domain through the northern boundary and forms a sea state with the aerodynamically smooth sea surfaces (Figure 5a,b) and with waves whose direction is strongly misaligned ($\theta = 60-160°$) with the local wind (Figure 5c,d). In particular, the reduced z_0 over swell persists under wind speed of up to 12 ms^{-1} (Figure 3a), despite the expectation that under such a high wind, the wind-waves would still strongly increase the aerodynamic roughness and stress.

Figure 6a,b compare the parameterized wind stress in WBF and WSDF. One can see from these plots a consistent difference in wind stress due to the inclusion of waves. Wind stress decreases sharply in wind speeds of 8-12 ms^{-1} over the northerly swell, where wave age >1.7. At the highest wind speed during the event, the percentage difference in wind stress magnitude exceeds 10%. Conversely, wind stress is increased in WBF by ≈4% over fully developed seas (wave age<1.7) and high winds, consistent with the increase in z_0 there (Figure 4c). By comparing to the direct momentum flux observations, we will determine in Section 4 if such reduced z_0 and τ over swell conditions at moderate to high wind speeds are consistent with the observations. As COARE3.5 does not consider the misaligned waves with winds, these conditions may constitute a source of uncertainty in the parameterized z_0 and τ via COARE3.5 WBF. As for the large wave age in the southeastern corner of the domain, it is concurrent with weaker winds (Figure 3a), and hence the assumptions about the swell under weaker wind seem valid in this region. This leads to a small difference in z_0 between WBF and WSDF.

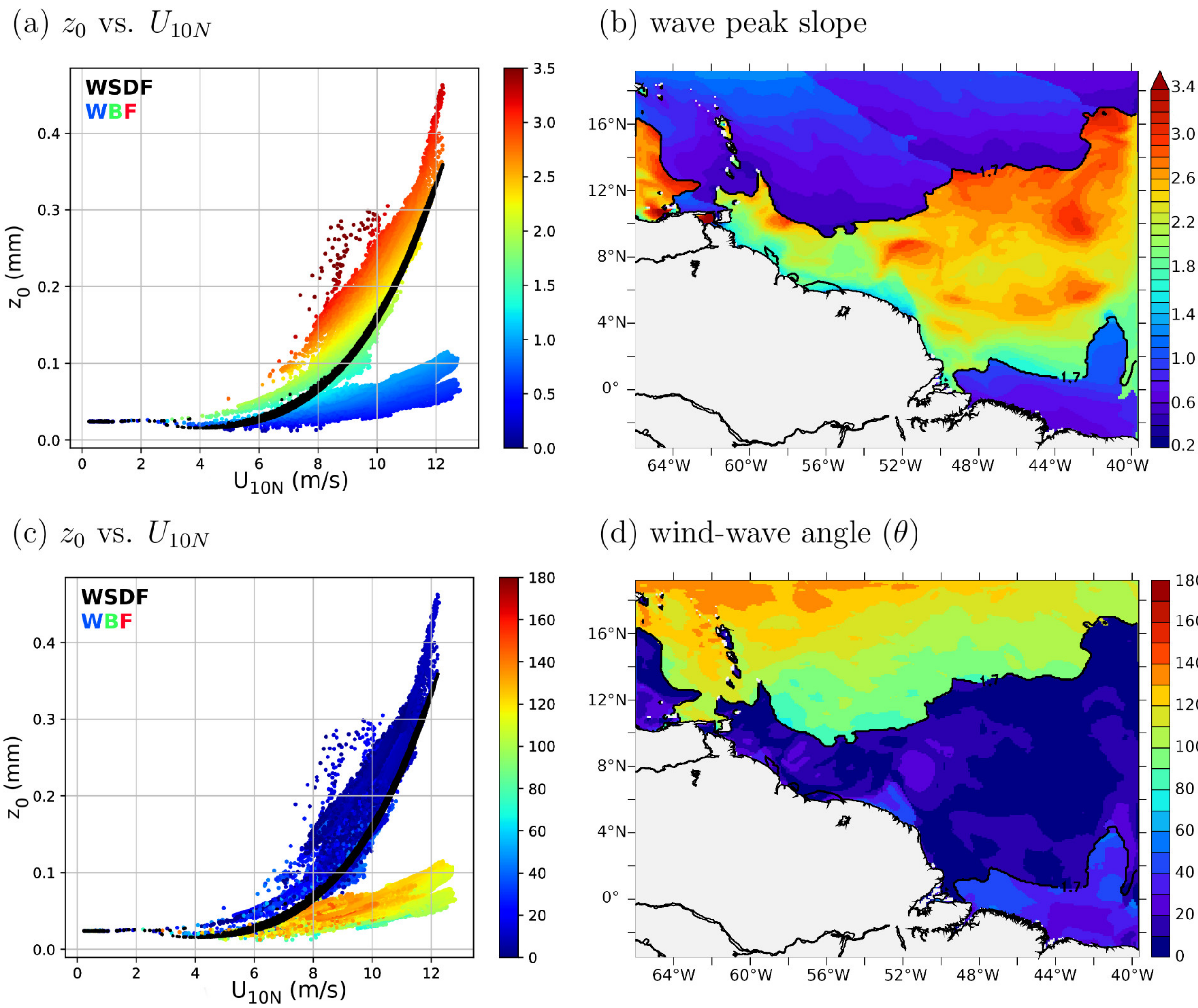

Figure 5. (a) Scatter plot of z_0 (mm) vs. U_{10N} (ms^{-1}) from WSDF in black and WBF color-coded to denote the corresponding wave peak slope (10^{-2}) defined as H_s/L_p where L_p is the peak wavelength. (b) A map of wave slope peak (10^{-2}), superposed with a contour of wave age = 1.7 on January 8, 2020 at 0600 UTC. (c,d) As in (a-b) except that colored scatters and shading denote the angle between the wind and wave directions (^{o}).

The altered stress directly influences the low-level winds via the surface drag. Here, we estimate the response in low-level winds at the lowest WRF model layer, at about 27 m above the sea surface. Figure 6c shows that the low-level wind is increased over the aerodynamically smooth sea surface due to swell by >0.5 ms^{-1}, accounting for 5-20% of the wind speed in WBF. In contrast, where young waves dominate in WBF, the wind stress is increased by 5% and the wind speed is decreased.

One relevant physical process that represents the air-sea momentum transfer affecting the winds and surface currents, is the wind work (P),

$$P = \frac{1}{\rho_o}\left(\overline{u_s \tau_x} + \overline{v_s \tau_y}\right), \tag{11}$$

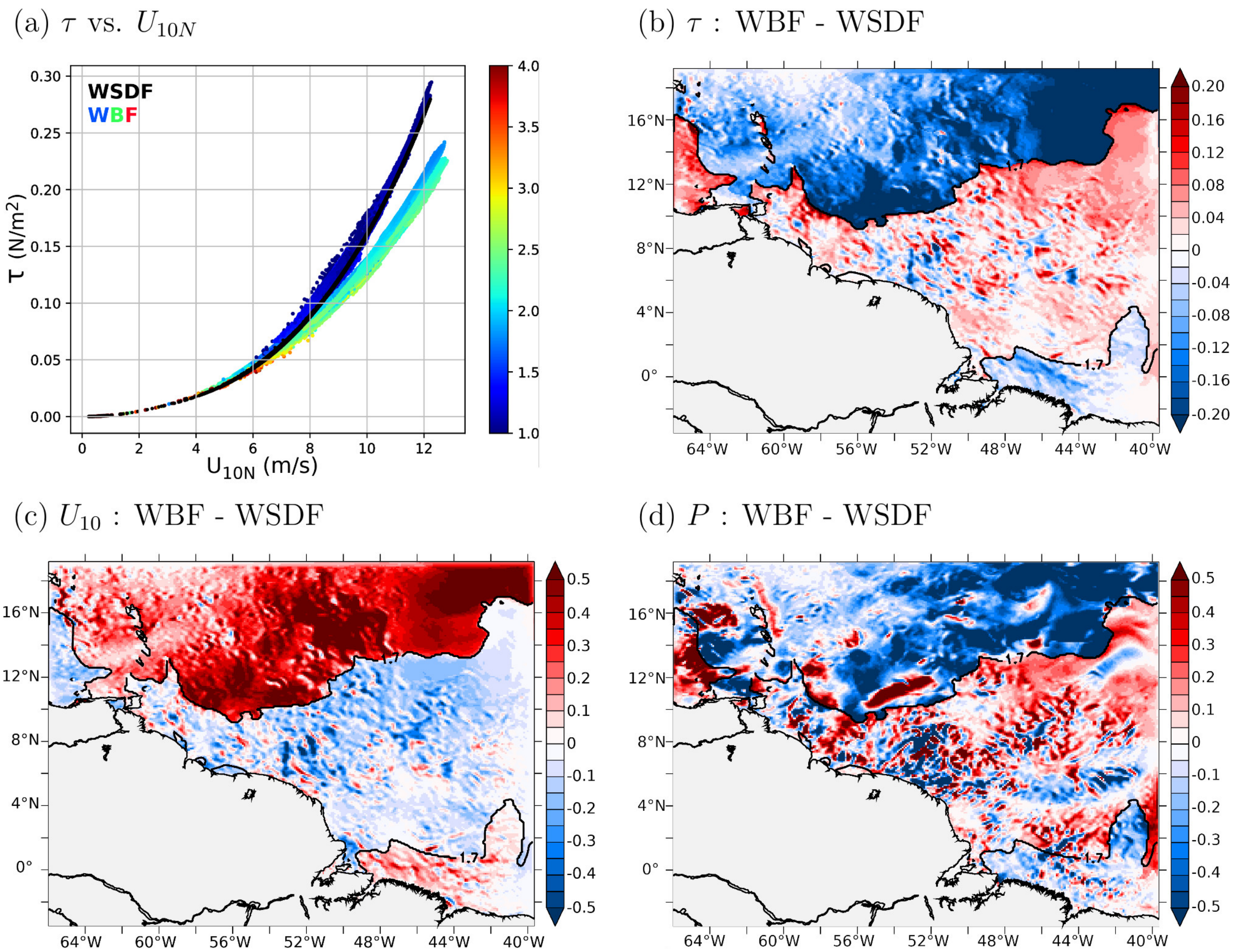

Figure 6. (a) Scatter plot of τ (Nm^{-2}) vs. U_{10N} (ms^{-1}) from WSDF in black and WBF color-coded to denote the corresponding wave age. (b,c,d) Difference maps between WBF and WSDF of (b) τ (10^{-1} Nm^{-2}), (c) U_{10} (ms^{-1}), and (d) wind work (P, $10^{-5}m^3s^{-3}$) on January 8, 2020 at 0600 UTC, superposed with a contour of wave age = 1.7.

where (u_s,v_s) are the surface current vectors, (τ_x,τ_y) are the wind stress vectors, and the overbar denotes the time-average. When P is positive, the mechanical work is done by the wind stress on the ocean surface currents, increasing the ocean kinetic energy (e.g., Wunsch, 1998). When negative, it represents the diversion of the ocean energy by the current to the wind, accelerating the low-level winds at the expense of weakened surface currents (e.g., Renault et al., 2016, 2017; Seo et al., 2019, 2021). Figure 6d shows the difference in P between WBF and WSDF for this snapshot. The region of reduced τ and increased low-level wind in the swell-dominated region is congruent with the region of the robust decrease in P, while the opposite is true in the Tradewind Alley region. The difference in P mainly reflects the changes in wind stress due to waves (Figure 6b).

4 Modeled and observed momentum fluxes during ATOMIC

Determining whether or not the parameterized z_0 and τ with WBF represents an improvement over WSDF requires a detailed comparison to direct covariance

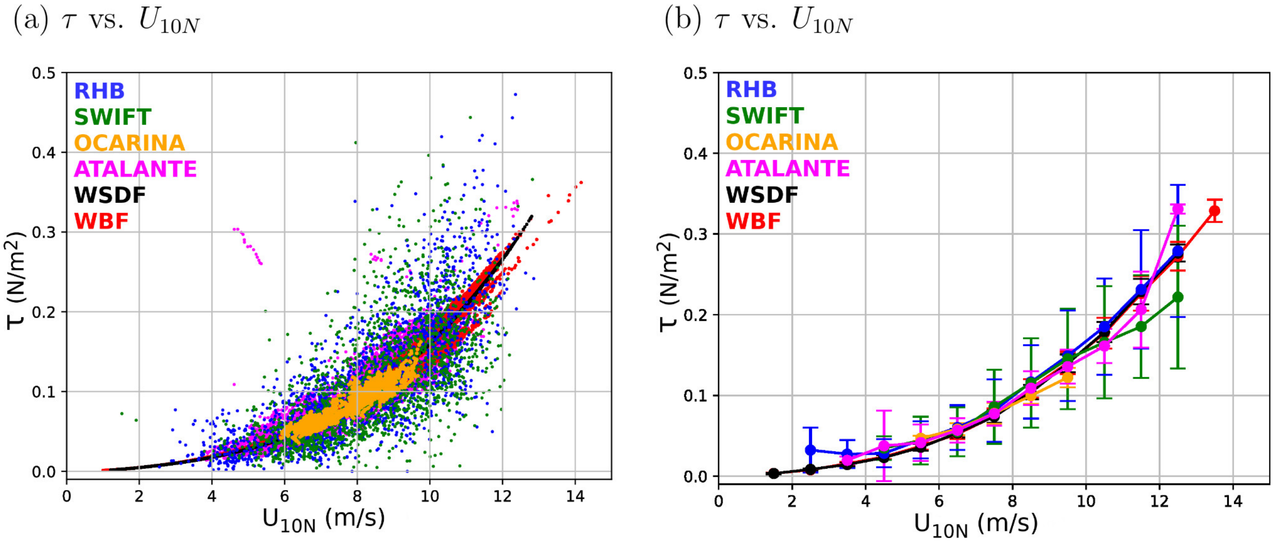

Figure 7. (a) Scatter plot comparing the two parameterized τ (Nm^{-2}) using COARE3.5 WSDF (black) and WBF (red) against the various types of measurements of τ (see Section 2e for a description of the various methodologies). (b) As in (a) except that measurements are bin-averaged with a wind speed bin-size of U_{10N} =1 ms^{-1}. The error bars represent ± 1 standard deviation. Only bins with more than 5 points are plotted.

stress measurements. In this section, we will compare the model simulation with the observations during the EUREC^{4}A/ATOMIC experiments to evaluate the accuracy of the wave-based parameterized τ and identify the regimes where further improvements might be needed.

Figure 7a compares the two modeled stresses to the observations. All observations and the two model simulations display the quadratic relationship of wind stress with wind speed. RHB and SWIFT, sampling the stress mainly in the Tradewind Alley region, produce greater scatter compared to ATALANTE and OCARINA, which were deployed further south in the Eddy Boulevard region (1a). The significant departure from this curve in the Tradewind Alley region may reflect the greater uncertainties in determining τ from these measurements. Between the model simulations, WBF produces a larger spread than WSDF, yet their averages at given wind speed are similar (Figure 7b). Overall, parameterized stresses by WSDF and WBF both agree well with the observations to within the observational errors during the campaign.

Figure 8a compares the histograms of the wave age from the WBF run to those from the SWIFT drifters and the RHB. It should be noted that in both the model and measurements, the wave age is estimated using the peak period (T_p). The observations and model simulation show the bi-modal distribution of wave age as was seen from the snapshot case in Section 3 (Figure 4a), with the first peak near wave age 1.7 and the secondary, much broader, peak between 2.5-3. The SWIFT observations (in red) capture a higher occurrence of young waves than the RHB observations or the WBF simulation. WBF also features a fatter tail of the distribution toward larger wave ages, indicating that the model overemphasizes the occurrences of swell and decaying waves compared to these observed estimates.

Given the wave age distributions, we then divide the distribution into 3 different "Regimes" to better understand the wave age-dependent z_0-wind speed and

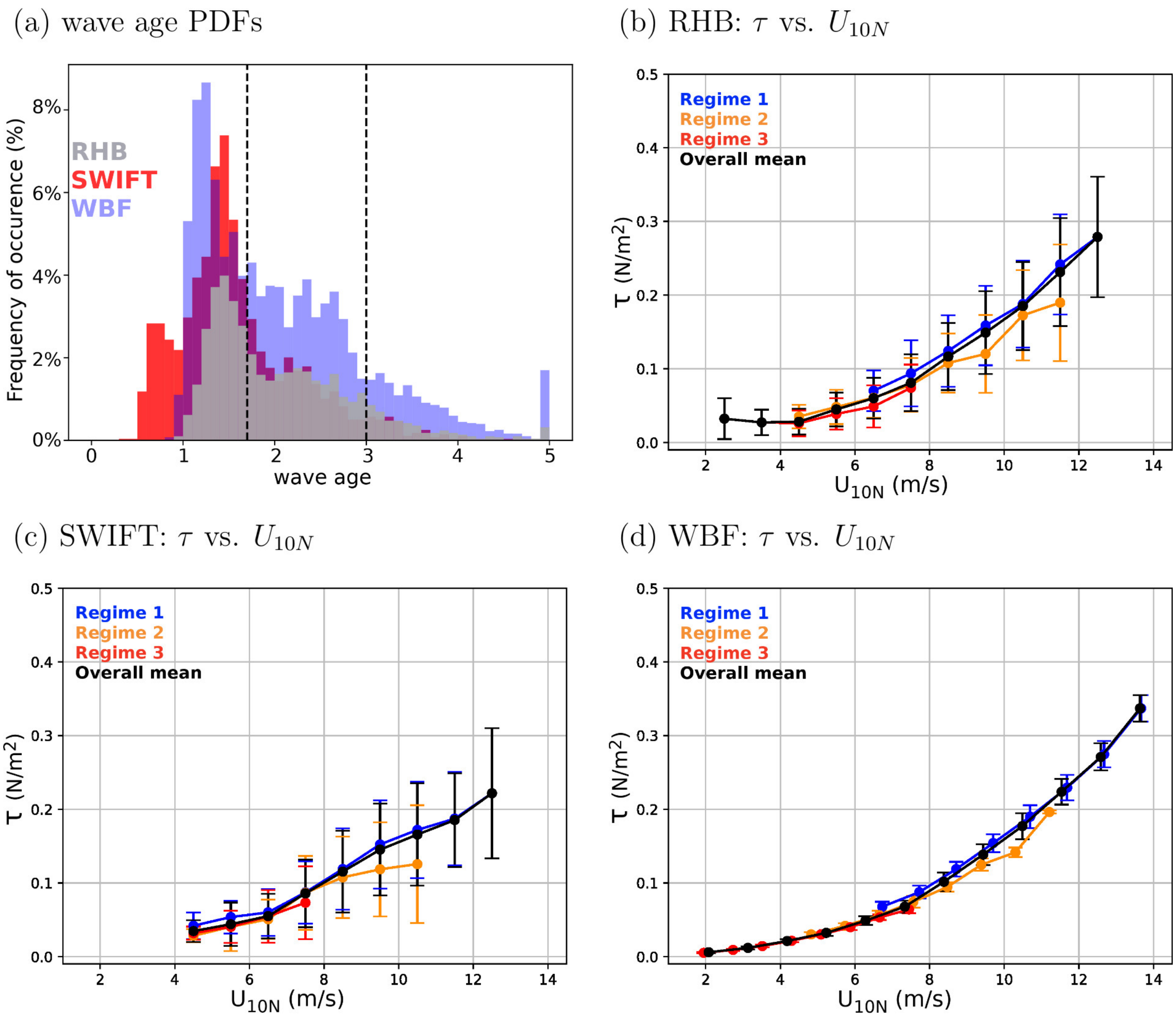

Figure 8. (a) Peak wave age distribution estimated from SWIFT (red), RHB (gray), and WBF (blue). Here, wave age is capped at 5. Three wave age regimes are defined: Regime 1 (blue) when wave age <1.7 denotes the young sea to fully developed sea, Regime 2 (orange) when wave age is between 1.7 and 3 indicates the mature to old sea, and Regime 3 (red) when wave age >3 represents the old sea and non-locally generated swell. (b-c) Binned scatter plots of τ (Nm^{-2}) vs. U_{10N} (ms^{-1}), color-coded to show the three different wave age Regimes, with the bin-average of 1 ms^{-1}. The error bars represent $\pm$ 1 standard deviation. Only bins with more than 5 points are plotted. The mean of all wave ages is shown in black. (d) As in (b) and (c) except from the WBF run. Here WBF is sampled along-track of the RHB and SWIFT.

τ-wind speed relationships. Regime 1 refers to young to fully developed seas, defined as when wave age <1.7, while Regime 2 indicates the mature to old sea, including mixed sea state, which is diagnosed as wave ages between 1.7 and 3. Finally, the old sea and non-locally generated swell characterizes Regime 3 estimated as when wave age > 3. When using the peak period, and to stay consistent throughout the paper, thresholds are kept the same. However, these thresholds are not necessarily universal but can vary in different times or regions under consideration.

The colored lines in Figures 8b and c show the bin-averaged surface stress from the RHB and the SWIFT from the 3 Regimes. The black lines denote the bin-averaged surface stress across all wave age regimes. Despite the significant error bars, which represent ± 1 standard deviation, one can observe the consistent relationship between the measured stress and the wind speed across different wave age. For example, the measured stress over Regime 1 (blue) is higher than the overall average (black) as the short-wind waves support the bulk of momentum exchanges. In contrast, the stress over Regime 2 (orange) and Regime 3 (red) is lower than the overall average, as the sea state is characterized by mixed and older seas. This sea state dependence of wind stress is also somewhat evident in the WBF simulation (Figure 8d) despite the smaller error bars likely due to smaller number of samples in the model, as discussed in Section 2d.

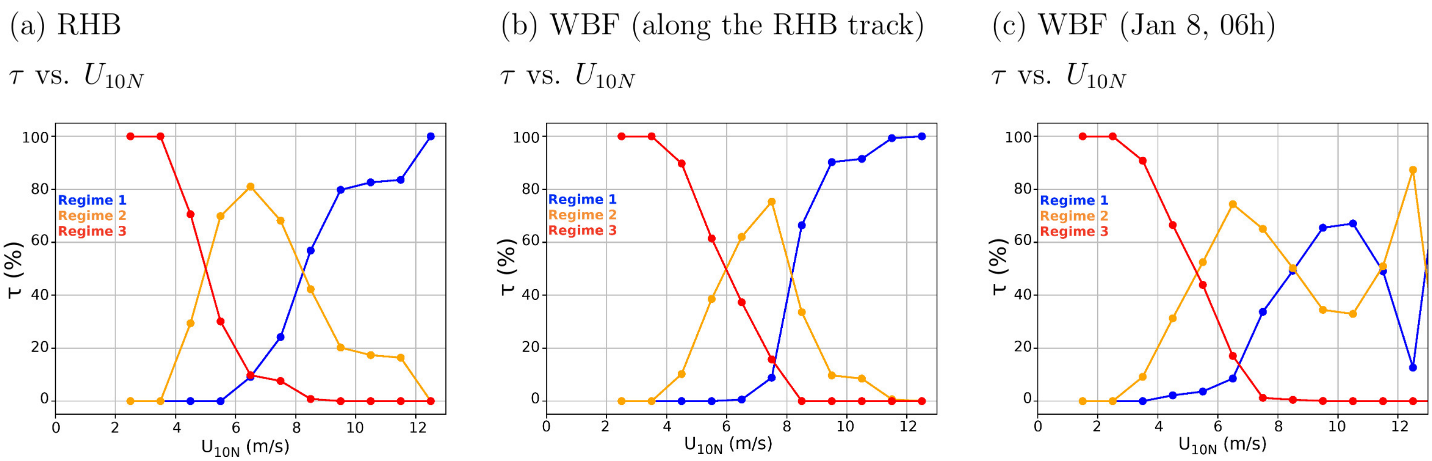

Figure 9. Percentage contribution of τ (%) by the three different wave age Regime at a given wind speed (bin averaged every 1 ms^{-1}) from (a) RHB, (b) WBF sampled along the RHB track between January 9 and February 13, 2020 and (c) WBF sampled over the whole model domain on January 8, 2020 at 0600 UTC. The different colors denote the different wave age categories described in Figure 8.

To further quantify this relationship, Figure 9a shows the percentage of stress supported by the different wave-age Regimes from the RHB observations, binned over 1 ms^{-1} intervals. Under 4 ms^{-1} wind speeds, the surface stress is mainly supported by Regime 3 (red), whereas above 8 ms^{-1}, Regime 1 (blue) dominates the contribution to the stress. Regime 2, which represents mixed sea conditions (orange), mainly supports the surface stress at low to moderate wind speeds (4-8 ms^{-1}) and contributes to less than 20% of the stress above 10 ms^{-1}. Figure 9b shows the same diagnostics, but for the WBF run sampled along the track of RHB. It shows that the WBF overall exhibits a similar fractional contribution to stress.

When the model is compared to the observations at this particular track, WBF appears to accurately characterize the observed stress relationship with wave age (See also Figure 8). However, if sampled over a broader region of the same mixed sea conditions from the model, a different result is obtained. Figure 9c shows the same results as Figure 9b, except that the entire model domain is sampled under the same synoptic condition examined in Section 3. It shows that the parameterized stress under 8-12 ms^{-1} wind speeds supported by Regime 2 (orange) is comparable to the stress supported by Regime 1 (blue) as also seen in Figure 6. In reality, short wind waves under such wind speeds should still support the increased stress despite

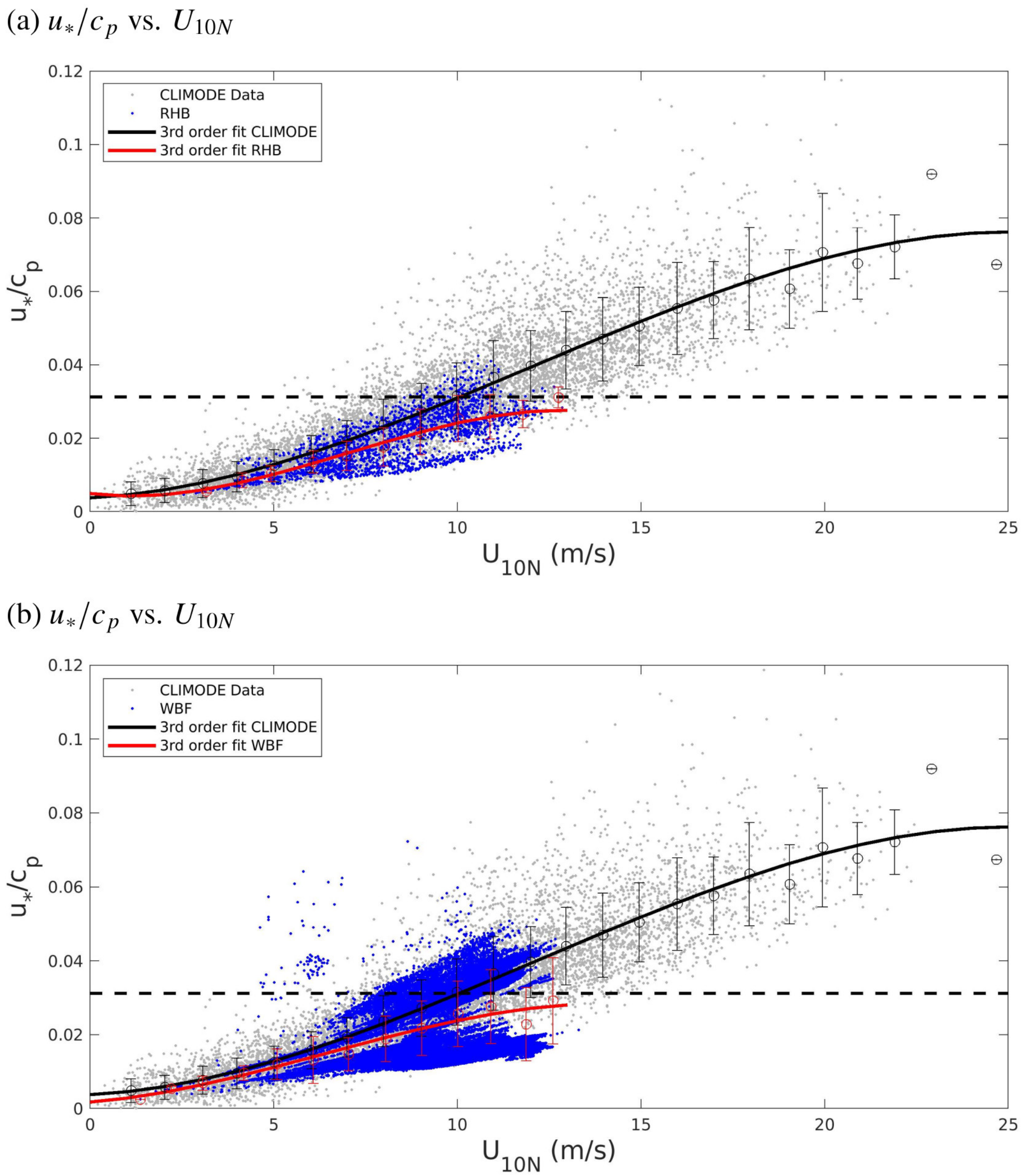

Figure 10. (a) Scatter plot of inverse peak wave age (u_*/c_p) vs. U_{10N} (ms^{-1}) for CLIMODE data (gray) and RHB data (a, blue). Bin-averages with the 1 standard deviation error bars are overlaid, at 1 ms^{-1} interval, along with the 3rd order fit (line) for CLIMODE (black) and RHB (red). The horizontal dashed line is $u_*/c_p = 0.03$, denoting the threshold for fully developed seas (equivalent to $c_p/U_{10N} = 1.2$). (b) As in (a) but RHB data is replaced with WBF, for the whole domain

on January 8, 2020 at 0600 UTC.

the higher wave age, we believe this is a form of deficiency in COARE3.5 WBF in representing the wind stress over mixed swell-dominated seas.

In fact, the COARE3.5's WBF was developed and tuned primarily by using the wave data collected from the extratropics, where sea state tends to be dominated by growing and fully-developed waves under high winds (see Figure 2 in Edson et al., 2013). Figure 10 compares the sea state used to tune COARE3.5, taken during the CLIMODE campaign (CLIVAR Mode Water Dynamic Experiment, Marshall et al., 2009), with the sea state observed by RHB during January-February 2020 and modeled in WBF on January 8, 2020 at 0600 UTC in the ATOMIC region. It shows the relationship between the inverse wave age and U_{10N}. Here, a low inverse wave age is indicative of decaying seas and swells. An inverse wave age of 0.03 (dashed line) is roughly equivalent to an equilibrium wave age of 1.2. As expected, the sea state captured in the ATOMIC region is very different and much older than the one used in COARE3.5. Therefore, the wind stress under moderate winds and swell dominated conditions observed here, and possibly in other tropical oceans, may not be currently well parameterized in the COARE3.5 WBF. The specific deficiency identified from this analysis is that, for mixed seas (Regime 2) where high wave age and moderately strong wind co-occur, the current COARE3.5 WBF overemphasizes the swell impact on wind stress, leading to the low-stress bias despite the moderately strong winds.

5 The revised wave-based formulation in COARE3.5

In the following, we present two experimental revisions to the z_0 formulation in the current COARE3.5 WBF for swell conditions coincident with moderate to high winds, the condition that is frequently observed in the northern ATOMIC region in the boreal winter. One method is to replace the peak wave period (T_p) with the mean wave period (T_m) in the definition of the phase speed and thus wave age, and another is to incorporate the effect of misaligned waves with local wind on aerodynamic roughness in the z_0 parameterization. In essence, these two observationally-guided approaches desensitize the impact of swell on z_0 and τ estimates at moderate winds and alleviate the low biases in the current COARE3.5 WBF. For this, we now return to the case study on January 8, 2020 as in Section 3.

5.1 The mean wave period

One possible approach to mitigate the overestimation of the swell impact on z_0 and τ under moderate to high winds is to use the wave's mean period, T_m, to calculate the average phase speed, c_m, in the wave age definition. This change is motivated by the finding that T_p does not accurately describe a mixed-sea state where swell and wind-sea co-exist, as shown in Figure 10. T_p can be also sensitive to the spectral shape of the wave energy and the chosen filter, while T_m can be reliably estimated from observations and WW3 as either an energy-weighted average period or zero-crossing period. A similar argument has been made recently by (Colosi et al., 2021) as they chose to use a wave age dependent computed with the mean period to construct the seasonal probability of swell over global oceans.

We carried out an additional coupled simulation, dubbed WBF_T_m, where T_p is replaced with T_m to get the mean phase speed of the waves c_m in Eq. 12:

$$z_{rough} = H_s D(\frac{u_*}{c_m})^B, \tag{12}$$

where D=0.39 and B=2.6, which have been tuned using the COARE3.5 set of observations. We will estimate T_m based on the zero-crossing period, as it is the one used to describe T_m in the observation. Figure 11 shows the same diagnostics as in Figure 10 but this time using c_m to calculate the inverse wave age in both the observations, CLIMODE and RHB, and the WBF_T_m run. The general trend of both sets of observations are now in good agreement (Fig. 11a). In WBF_T_m, the use of c_m in eq. 12 alleviates the bias over the mixed sea (Regime 2) (Figure 10b vs. Fig. 11b) and shows a better agreement of the general trends from the observations.

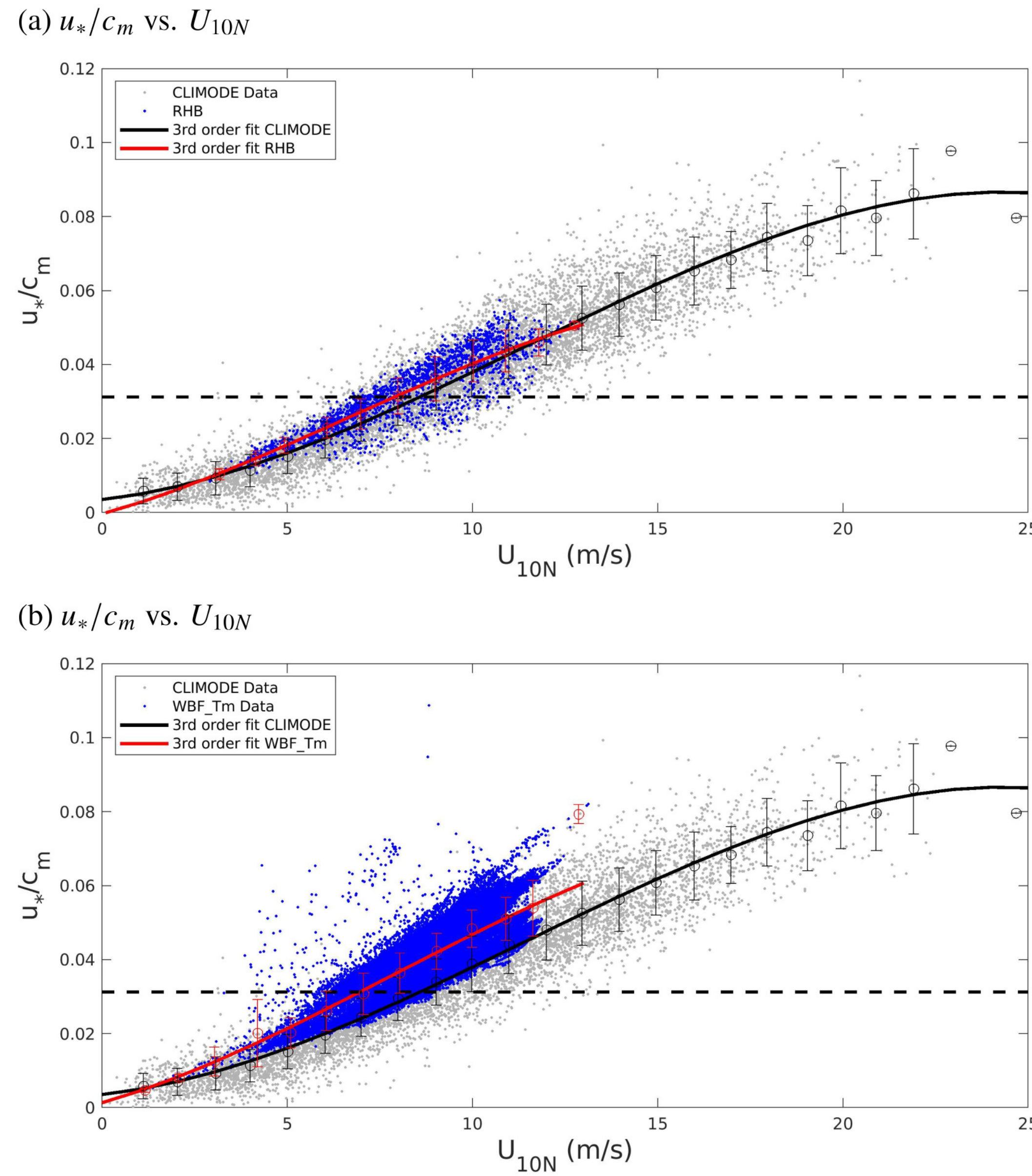

Figure 11. (a) As in Figure 10a, but with inverse mean wave age (u_*/c_m). The dashed line is $u_*/c_m = 0.03$, denoting the threshold for fully developed seas (equivalent to $c_m/U_{10N} = 1.2$). (b) As in Figure 10b except for showing the result from WBF_T_m

Further refinement of coefficients in eq. 12 will be addressed in more detail in the future release of the COARE4.0 algorithm.

Figure 12a shows the PDF of wave age for RHB (gray), SWIFT (red), and WBF_T_m (blue) computed using T_m. This figure should be compared to Figure 8a where RHB, SWIFT and WBF wave age PDFs were computed using T_p. Similar to Figure 8a, wave age is capped at 5 to show the tail of the distribution. In contrast to the bi-modal distribution of wave age with the pronounced secondary peak of wave age estimate with T_p, the use of T_m effectively removes this secondary peak in both the model and observations, yielding a markedly different distribution with an overall prevalence of younger sea state. We adjusted the different categories of

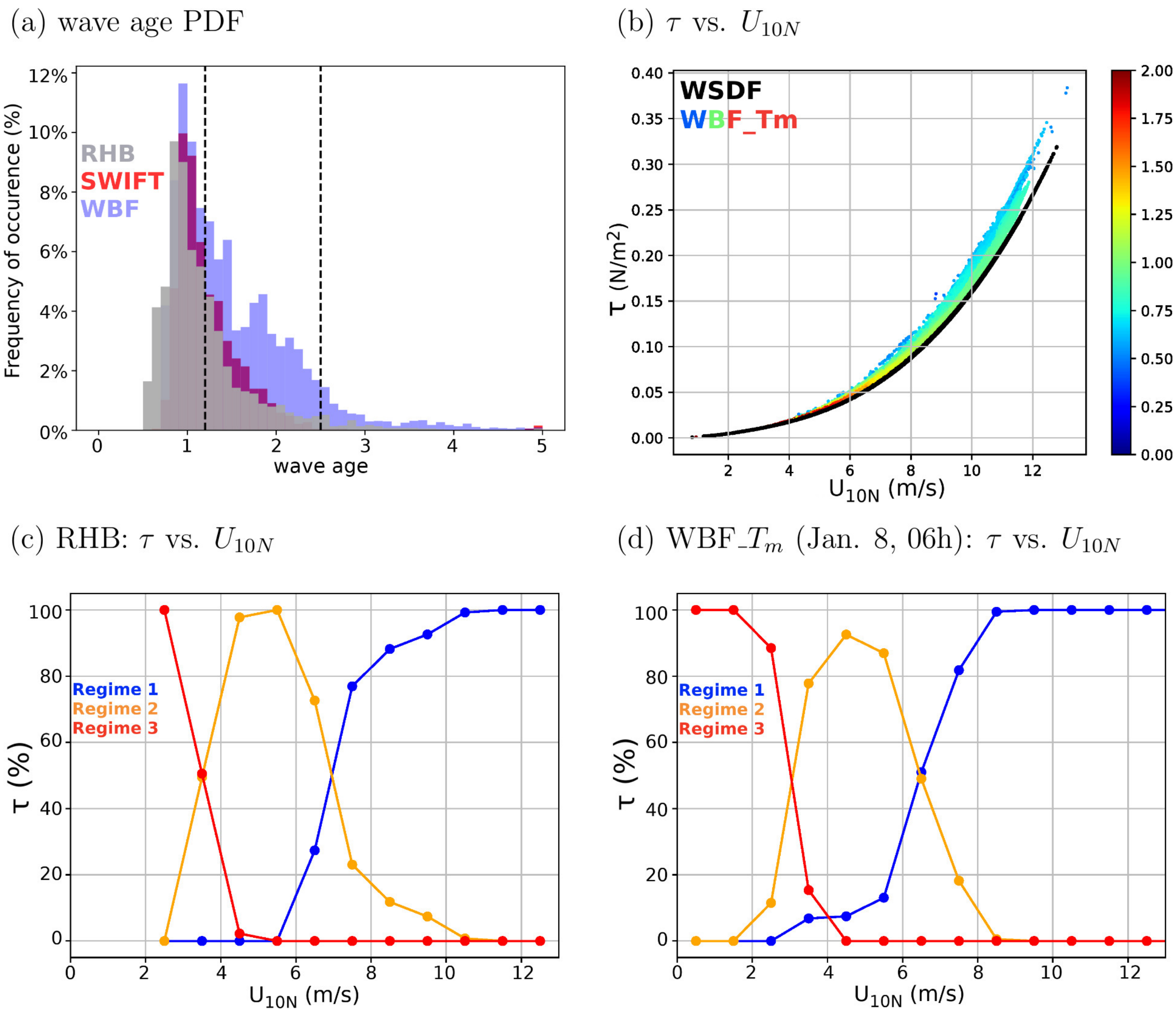

Figure 12. (a) Mean wave age distributions estimated from RHB (gray), SWIFT (red), and WBF_T_m (blue). WBF_T_m is sampled along-track of the RHB and SWIFT. (b) Scatter plot of τ (Nm^{-2}) vs. U_{10N} (ms^{-1}) from WSDF in black and WBF_T_m color-coded to denote the corresponding wave age on January 8, 2020 at 0600 UTC. (c,d) As in Figure 9a,c, except that the wave age is defined with T_m for (c) RHB and (d) WBF_T_m.

wave age defined previously to fit the new wave age distribution based on T_m. Figure 12b shows τ on January 8, 2020 at 0600 UTC from WBF_T_m, with wave age color-coded. The cluster of low z_0 with high wave age seen in Figure 4b is eliminated in WBF_T_m, because of the elevated z_0 and τ under moderate to high wind speeds. Finally, Figure 12c,d, to be compared to Figure 9a,c shows the percentage of τ supported by each category of wave age for RHB and for WBF_T_m, respectively. With the use of T_m, WBF_T_m agrees well with RHB concerning the fractional contribution from each sea state to the surface stress. Particularly over 7 ms^{-1}, most of the contribution to τ now comes from the wind sea (blue), whereas the contribution of mature seas and swell subsides rapidly with the increased wind speeds. This is a clear improvement from τ parameterized using T_p (Figure 9c) and is much more consistent with the observations (Figures 9a, 12c).

5.2 Including the (mis)aligned wind-wave directions

As discussed in Section 2, the COARE3.5 assumes the wave stress as a scalar roughness parameter, and hence the direction of wave-stress vectors is aligned with the mean wind vectors. However, wave stress and mean wind vectors can be misaligned under various conditions, including under rapidly translating storms (e.g., S. S. Chen et al., 2013), near strong vorticity and divergence gradients and density fronts (e.g., Villas Bôas & Young, 2020), or over mixed seas where wind waves and swells co-exist under high winds. Such nonequilibrium wave motions can influence wave slope, roughness length, and wind stress (Janssen, 1991; Rieder et al., 1994; Zou et al., 2019; Patton et al., 2019; Porchetta et al., 2021; Deskos et al., 2021). Here, we attempt to incorporate the directionality of the wind and waves following Patton et al. (2019) and Porchetta et al. (2019), such that

$$z_{rough} = H_s D cos(a\theta)(\frac{u_*}{c_p})^{B cos(b\theta)}. \tag{13}$$

D and B are the coefficients taken from COARE3.5 (See Eq. 8), while the coefficients $a = 0.4$ and $b = 0.32$ are adopted from (Porchetta et al., 2019). In principle, all these coefficients require site-specific tuning. For example, (Porchetta et al., 2019) used the high wind conditions observed from the FINO platform in the North Sea and the Air-Sea Interaction Tower (ASIT) in the New England Shelf, which represents different wind speed and wave age conditions from the trade-wind and swell-dominated tropical oceans as in the ATOMIC domain. Additional tuning exploiting direct momentum flux measurements would be needed to develop a refined set of coefficients for the tropical oceans. This is beyond the scope of the study. Using this new formulation, we conducted an additional coupled experiment, dubbed WBF_θ, which is to be compared to the default wave-based formulation in COARE3.5, where $\theta = 0$.

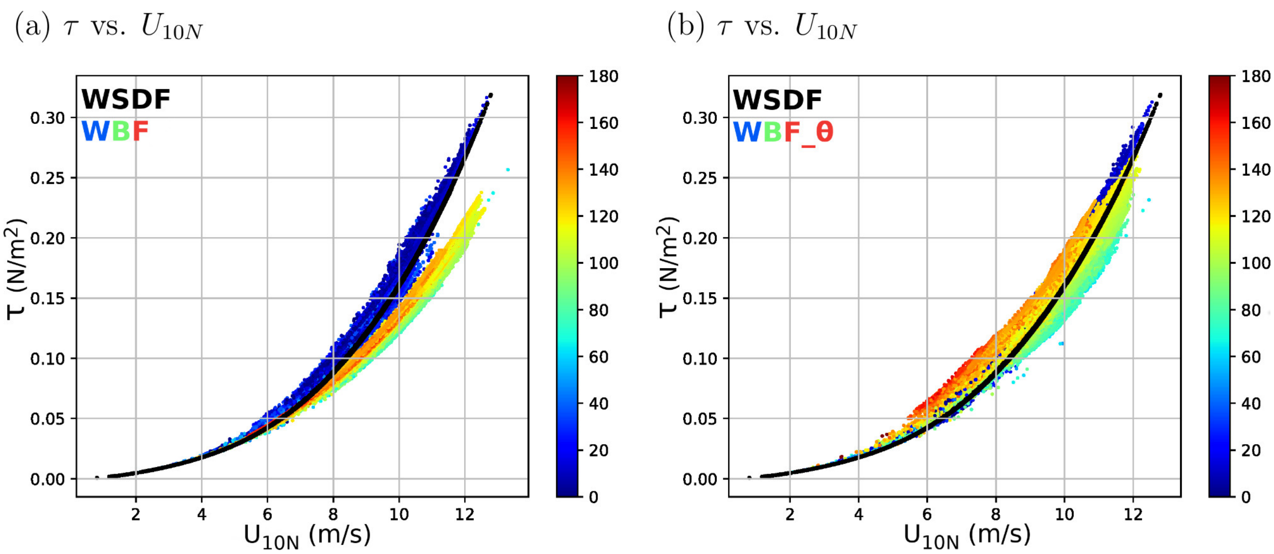

Figure 13. (a) Scatter plot of parameterized τ (Nm^{-2}) vs. U_{10N} (ms^{-1}) from WSDF in black and WBF color-coded to denote the corresponding wind-wave angle (θ) on January 8, 2020 at 0600UTC. Note that in the z_0 formulation in WBF assumes $\theta = 0$. (b) As in (a) except from WBF_θ, where θ is treated as a non-zero quantity in the z_0 formulation.

Figure 13a compares the parameterized τ, color-coded by the angle (θ) between the wind direction and peak wave direction in WBF. It shows that the lower τ from WBF compared to WSDF (and also observations) occurs when the swell waves are strongly misaligned with winds (e.g., $\theta > 60\text{-}90^o$). This indicates that the assumption of $\theta = 0$ in WBF can be attributed to the lower τ. When the directional misalignment is considered in the roughness length parameterization in COARE3.5 (Figure 13b), τ over the misaligned waves has been effectively elevated as the waves opposing the wind increase the surface drag. This is shown to reduce the low τ bias significantly.

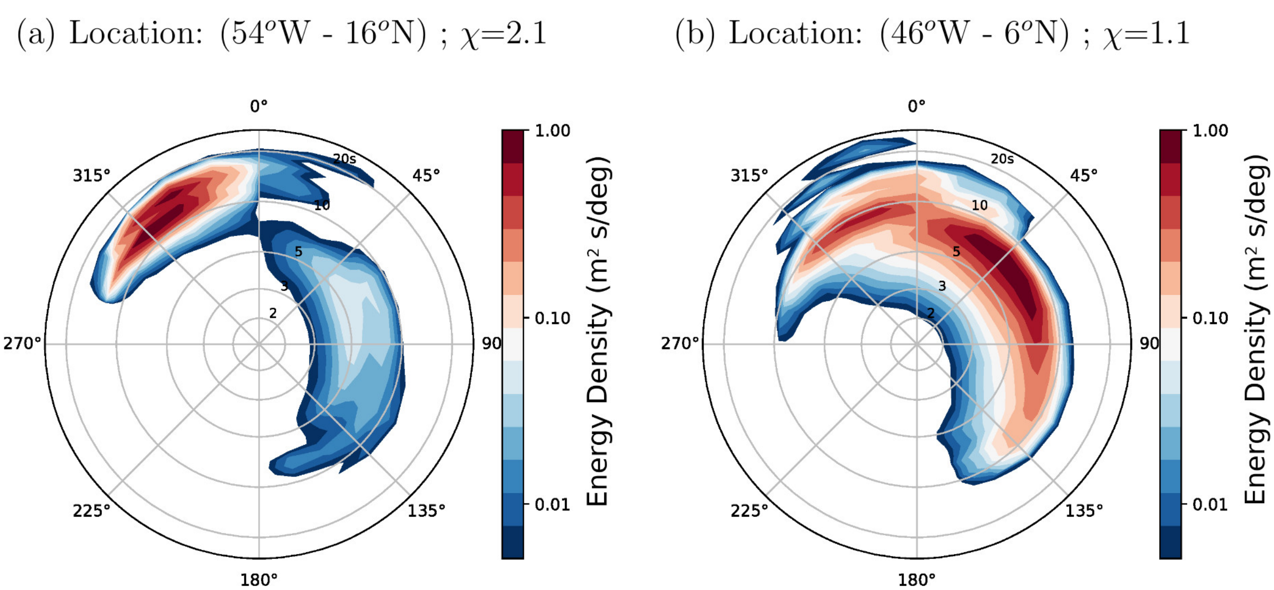

Figure 14. Normalized wave spectrum energy density ($m^2 sdeg^{-1}$) plotted in period (s) space from (a) one point in the northern part of the domain under swell influence and (b) one point in the center part of the domain on January 08, 2020 at 0600UTC for WBF.

Here, the alignment between wind and waves has been defined only by using the wave peak direction. Figure 14 compares the normalized wave spectrum energy density ($m^2 sdeg^{-1}$) shown in the period space between one grid point in the northern part of the domain under swell regime (Fig. 14a) and another grid point in the center part of the domain under wind waves regime for WBF. Both are sampled on January 08, 2020 at 0600UTC. On the northern grid point where the wave age was 2.1, Figure 14a shows the strong swell signal (with the periods of 10-20s) from the northwest direction. It does also show a large directional spreading, due to the concurrent shorter period wind waves (2-10s) originating from the northeast, east, and southeast direction. However, the energy density from the shorter-period waves is much weaker. In the center of the domain (Figure 14b), where the sea state is dominated by wind-waves and waves near equilibrium (the wage here is 1.1), the directional spreading is also quite large, but with higher energy in the wind waves and weaker energy in the swell.

The sea state in this region appears to be mixed ubiquitously between wind waves and swell in winter, leading to a large wave directional spreading. However, since the peak energy density is well separated between the swell (in the northern point, Fig. 14a) and the wind waves (in the southern point, Fig. 14b), we anticipate that the use of waves' direction variance in the bulk formula or the spectrally-averaged wave direction in the bulk formula, would yield qualitatively similar results. For this reason, in the present study, only the peak direction of the waves is used to account for the misaligned wave effect on z_0 in COARE. However, it is possible that by using the peak wave direction we would grossly underrepresent some unresolved processes contributing to the directional spread of waves, and its impact on z_0.

6 Conclusion

This study investigated the role of surface waves in surface roughness length (z_0) and surface stress (τ) in the persistent and strong trade winds and swell-dominated Northwestern Tropical Atlantic Ocean during the boreal winter season. The main objective is to evaluate how accurately the air-sea momentum flux is represented in advanced bulk flux algorithms such as COARE3.5 when compared to the direct surface flux measurements. In this investigation, estimated z_0 and τ from four different SCOAR ocean-atmosphere-wave coupled model simulations are analyzed. The results show that the estimated z_0 and τ differences strongly depend on wind speeds and wave age regimes. Wind sea or fully-developed sea under high winds are characterized by the enhanced wave slope and choppy surface (Figure 5b), which effectively increases the surface drag, and τ. The increased surface drag decelerates the near-surface winds (Figure 6c).

However, in the mixed sea condition, where moderate to high wind speeds (10 to 12 ms^{-1}) co-occur with decaying swell, the WBF tends to underestimate z_0 compared to the WSDF and τ compared to the measurements. The weak stress then accelerates the near-surface wind speed by 5% over the region of negative change in wind work (Figure 6d). The sea state, in this high wave age region, is strongly misaligned with the local wind (Figure 5d), indicating the presence of remotely-generated swell. However, despite the swell-dominated sea state, the observations suggest that the wind seas in this mixed sea condition should continue to support the momentum flux due to moderate-to-high wind speeds, thereby increasing τ with wind speed (Figure 7).

The different approaches were explored in this study to alleviate the low-stress bias in the COARE3.5 WBF under the mixed sea regime. The first approach involves re-defining wave age using the mean period of the waves to more accurately represent the wave period in the mixed sea condition (Figure 4a). The second approach takes advantage of the fully coupled model by considering the directionality of waves with respect to winds (Eq. 12), the vital missing process in the current COARE3.5 WBF and many numerical modeling studies except for a limited number of Large Eddy Simulations (LES) and offshore wind energy studies (See Review by Patton et al., 2019). Our results show that both approaches produce equivalent results by effectively boosting z_0 and τ under the misaligned waves under moderate-to-high winds. Since both methods yield equivalent results, accounting for both (peak direction and wave mean period), without more dedicated tuning with the measurements, produces too strong correction for the low bias (not shown). Finally, it is important to note that these improvements are most likely to be site-dependent, as we are only using limited observations in one specific region. Moreover, the improvement of the parameterization is mostly over specific regimes of wind and waves where the original parameterization was deficient.

Our analysis reveals a notable deficiency in the ocean-wave and wave-atmosphere coupling components of the coupled model, which guides the direction of our future investigation. That is, the frequency of swell simulated by the coupled WW3 model is overestimated compared to the in situ observations (Figure 8a), more so with the use of peak wave period but nonetheless noticeable with the use of mean period. Since the wave model provide the parameters required by the WBF, some of the issues described above are a result of inaccurate inputs as well as problems with the parameterization. The tendency toward the higher wave age indicates that the model under-represents critical dissipation mechanisms of the swell energy, and waves in general, which likely have contributed to the low-stress bias. There are at least two possible factors to consider.

First, the primary loss of swell energy is to the atmosphere in situations where the swell waves outrun the winds or propagate in the opposite direction to the local wind (e.g., M. Donelan, 1999; Rascle et al., 2008; Kahma et al., 2016; Liu et al., 2017). Tropical oceans, including our study region, have many low-wind regimes, where the wave-driven low-level wind jet (Harris, 1966) and turbulent mixing in the MABL (Kantha, 2006; Ardhuin & Jenkins, 2006; A. V. Babanin, 2006) constitute important sources for attenuation of the swell energy (Ardhuin et al., 2009; S. Chen et al., 2019). It is quite possible that the processes related to the upward flux of momentum and energy over swell are not adequately captured in our coupled wind-wave model. Previous studies find that the wave-driven wind jet is at heights of 5-10 m (Sullivan et al., 2008; Smedman et al., 2009). However, our experiments used the default vertical grid system in WRF, where the wind at the lowest height of the model is typically 30–50 m. The WRF PBL scheme expects this level to be within the constant-flux layer, where similarity theory is applied (Aligo et al., 2009; Shin et al., 2012). Yet, this level can be above the surface layer, especially in the low-wind and stable boundary layer conditions, as often observed in the northern part of the ATOMIC domain. If the turbulent mixing between the lowest model level and the swell at the sea surface is weak, the upward energy and momentum fluxes from the swell to the wind are likely to be under-represented. This might have been exacerbated by using a local PBL scheme (MYNN) in our model.

Moreover, parameterizations for the so-called negative wind input exist in standalone WW3 model through the use of the source term packages of wind input (M. A. Donelan et al., 2006; Ardhuin et al., 2010; A. Babanin, 2011; Rogers et al., 2012; Liu et al., 2017, 2019). With this, the standalone WW3 model forced with winds should better capture the loss of energy of swell waves. Yet, it is unclear how such parameterizations should be incorporated into the coupled model, as they do not represent the actual gain of momentum by the wind from the swell. Our future work will focus on adequately representing the near-surface wind responses to swell waves in the atmospheric model.

Secondly, the wave breaking and the induced near-surface mixing would influence the wave energy growth and attenuation (e.g., Kudryavtsev et al., 2014). Also, Iyer et al. (2022), using the SWIFT drifters deployed during the ATOMIC campaign, showed that wave-current interactions can generate significant spatial and temporal variability in momentum fluxes in this region. However, here, since the current study does not include wave-ocean coupling, the question about the impacts of ocean-wave coupling on the skill of the simulated wave fields cannot be addressed. This is a subject of ongoing efforts.

7 Open Research

The observational datasets from the ATOMIC and EUREC^{4}A experiments (Stevens et al., 2021) are available freely on `https://observations.ipsl.fr/aeris/eurec4a/\#/`. ERA5 Atmospheric hourly reanalyses were made available by the Copernicus Climate Change Service (Hersbach et al., 2018a, 2018b). Mercator Ocean International daily analyses (Lellouche et al., 2018) were made available by the Copernicus Marine Environment Monitoring Service on `https://doi.org/10.48670/moi-00016`. Global 3-hourly spectral wave analyses were made available by Ifremer (Rascle & Ardhuin, 2013) on a FTP server at ftp://ftp.ifremer.fr/ifremer/ww3/HINDCAST/GLOBAL; WaveWatchIII model (The WAVEWATCH III Development Group, 2016) is available at `https://github.com/NOAA-EMC/WW3`. WRF model (Skamarock et al., 2008) is available at `https://github.com/wrf-model/WRF`. ROMS model (Shchepetkin & McWilliams, 2005) is also freely available at `https://github.com/kshedstrom/roms`. The SCOAR (Seo et al., 2007) code is available at `https://github.com/hyodae-seo/SCOAR`. Finally, the original versions of COARE3.5 (Edson et al., 2013) bulk formula is available at `https://github.com/NOAA-PSL/COARE-algorithm`.

Acknowledgments

This research was supported by NOAA (NA19OAR4310376), NASA (80NSSC21K1524), and NSF (OCE-2148120). HS also acknowledges the additional support from NSF (OCE-2022846) and NOAA (NA17OAR4310255, NA22OAR4310598). JE is partially supported by NSF (OCE-1829957). The computing resources were provided by the WHOI High-Performance Computing Facility. The authors thank the ATOMIC and EUREC^{4}A team for providing the observational datasets (https://observations.ipsl.fr/aeris/eurec4a/#/). The authors also thank Elizabeth Thompson, Jim Thomson, Suneil Iyer, Ludovic Bariteau, Kyla Drushka, Chris Fairall and Denis Bourras for their insightful comments.

References

Aligo, E. A., Gallus, W. A., & Segal, M. (2009). On the impact of WRF model vertical grid resolution on Midwest summer rainfall forecasts. *Wea. Forecasting*, *24*, 575–594.

Ardhuin, F., Chapron, B., & Collard, F. (2009). Observation of swell dissipation across oceans. *Geophys. Res. Lett.*, *36*(6). doi: 10.1029/2008GL037030

Ardhuin, F., Gille, S. T., Menemenlis, D., Rocha, C. B., Rascle, N., Chapron, B., . . . Molemaker, J. (2017). Small-scale open ocean currents have large effects on wind wave heights. , *122*, 4500-4517. doi: 10.1002/2016JC012413

Ardhuin, F., & Jenkins, A. D. (2006). On the Interaction of Surface Waves and Upper Ocean Turbulence. *Journal of Physical Oceanography*, *36*(3), 551 - 557. doi: 10.1175/JPO2862.1

Ardhuin, F., O'Reilly, W. C., Herbers, T. H. C., & Jessen, P. F. (2003). Swell Transformation across the Continental Shelf. Part I: Attenuation and Directional Broadening. *J. Phys. Oceanogr.*, *33*(9), 1921-1939. doi: 10.1175/1520-0485(2003)033⟨1921:STATCS⟩2.0.CO;2

Ardhuin, F., Rogers, E., Babanin, A. V., Filipot, J.-F., Magne, R., Roland, A., . . . Collard, F. (2010). Semiempirical Dissipation Source Functions for Ocean Waves. Part I: Definition, Calibration, and Validation. *J. Phys. Oceanogr.*, *40*(9), 1917-1941. doi: 10.1175/2010JPO4324.1

Ardhuin, F., & Roland, A. (2012). Coastal wave reflection, directional spread, and seismoacoustic noise sources. *J. Geophys. Res.*, *117*(C11). doi: 10.1029/2011JC007832

Babanin, A. (2011). *Breaking and Dissipation of Ocean Surface Waves.* Cambridge University Press. doi: 10.1017/CBO9780511736162

Babanin, A. V. (2006). On a wave-induced turbulence and a wave-mixed upper ocean layer. *Geophysical Research Letters*, *33*(20). doi: https://doi.org/10.1029/2006GL027308

Battjes, J., & Janssen, J. (1978, Jan.). Energy loss and set-up due to breaking of random waves. *Coastal Engineering Proceedings*, *1*, 32. doi: 10.9753/icce.v16.32

Bourras, D., Branger, H., Luneau, C., Reverdin, G., Speich, S., Geykens, N., . . . Clémençon, A. (2020). EUREC4A-OA_OCARINA : OCARINA

Air-Sea Flux Data. *SEANOE*. (Accessed 23 December 2021) doi: https://doi.org/10.17882/77479

Bourras, D., Geyskens, N., Reverdin, G., Clémençon, A., Barrois, H., Branger, H., & Luneau, C. (2020). EUREC4A-OA experiment: Air-Sea Flux Mast Data. *SEANOE*. (Accessed 23 December 2021) doi: https://doi.org/10.17882/77341

Bôas, A. B. V., Cornuelle, B. D., Mazloff, M. R., Gille, S. T., & Ardhuin, F. (2020). Wave–Current Interactions at Meso- and Submesoscales: Insights from Idealized Numerical Simulations. *Journal of Physical Oceanography*, *50*(12), 3483 - 3500. doi: 10.1175/JPO-D-20-0151.1

Charnock, H. (1955). Wind stress on a water surface. *Quart. J. Roy. Meteor. Soc.*, *81*(350), 639-640. doi: 10.1002/qj.49708135027

Chen, F., & Dudhia, J. (2001). Coupling an Advanced Land Surface–Hydrology Model with the Penn State–NCAR MM5 Modeling System. Part I: Model Implementation and Sensitivity. *Monthly Weather Review*, *129*(4), 569 - 585. doi: 10.1175/1520-0493(2001)129⟨0569:CAALSH⟩2.0.CO;2

Chen, S., Qiao, F., Jiang, W., Guo, J., & Dai, D. (2019). Impact of Surface Waves on Wind Stress under Low to Moderate Wind Conditions. *Journal of Physical Oceanography*, *49*(8), 2017 - 2028. doi: 10.1175/JPO-D-18-0266.1

Chen, S. S., Zhao, W., Donelan, M. A., & Tolman, H. L. (2013). Directional wind–wave coupling in fully coupled atmosphere–wave–ocean models: Results from cblast-hurricane. *Journal of the Atmospheric Sciences*, *70*(10), 3198 - 3215. doi: 10.1175/JAS-D-12-0157.1

Chou, M.-D., & Suarez, M. J. (1999). A Solar Radiation Parameterization for Atmospheric Studies. *Technical Report Series on Global Modeling and Data Assimilation*, *15*.

Colosi, L. V., Villas Bôas, A. B., & Gille, S. T. (2021). The seasonal cycle of significant wave height in the ocean: Local versus remote forcing. *Journal of Geophysical Research: Oceans*, *126*(8), e2021JC017198. doi: https://doi.org/10.1029/2021JC017198

Csanady, G. T., & Gibson, M. (2001). *Air-Sea Interaction: Laws and Mechanisms.* Cambridge University Press. doi: 10.1017/CBO9781139164672

Deskos, G., Lee, J. C. Y., Draxl, C., & Sprague, M. A. (2021). "review of wind–wave coupling models for large-eddy simulation of the marine atmospheric boundary layer". *Journal of the Atmospheric Sciences*, *78*(10), 3025 - 3045. doi: 10.1175/JAS-D-21-0003.1

Donelan, M. (1999). Wind-induced growth and attenuation of laboratory waves. *In: Institute of Mathematics and Its Applications Conference Series*, *69*, Oxford;Clarendon, 183-194.

Donelan, M. A., Babanin, A. V., Young, I. R., & Banner, M. L. (2006). Wave-Follower Field Measurements of the Wind-Input Spectral Function. Part II: Parameterization of the Wind Input. *Journal of Physical Oceanography*, *36*(8), 1672 - 1689. doi: 10.1175/JPO2933.1

Drennan, W. M., Graber, H. C., Hauser, D., & Quentin, C. (2003). On the wave age dependence of wind stress over pure wind seas. *Journal of Geophysical Research: Oceans*, *108*(C3). doi: https://doi.org/10.1029/2000JC000715

Edson, J., Jampana, V., Weller, R., Bigorre, S., Plueddemann, A., Fairall, C., ... Hersbach, H. (2013). On the exchange of momentum over the open ocean. *Journal of Physical Oceanography*, *43*(8), 1589 - 1610. doi: 10.1175/JPO-D-12-0173.1

Egbert, G. D., & Erofeeva, S. Y. (2002). Efficient inverse modeling of barotropic ocean tides. *Journal of Atmospheric and Oceanic Technology*, *19*(2), 183 - 204. doi: 10.1175/1520-0426(2002)019⟨0183:EIMOBO⟩2.0.CO;2

Fairall, C. W., Bradley, E. F., Hare, J. E., Grachev, A. A., & Edson, J. B. (2003). Bulk parameterization of air-sea fluxes : Updates and verification for the COARE algorithm. *Journal of Climate*, *16*, 571-591.

Fairall, C. W., Bradley, E. F., Rogers, D. P., Edson, J. B., & Young, G. S. (1996). Bulk parameterization of air-sea fluxes for tropical ocean-global atmosphere coupled-ocean atmosphere response experiment. *Journal of Geophysical Research: Oceans*, *101* (C2), 3747-3764. doi: https://doi.org/10.1029/95JC03205

Hanley, K. E., & Belcher, S. E. (2008). Wave-Driven Wind Jets in the Marine Atmospheric Boundary Layer. *Journal of the Atmospheric Sciences*, *65* (8), 2646 - 2660. doi: 10.1175/2007JAS2562.1

Harris, D. L. (1966). The Wave-Driven Wind. *Journal of Atmospheric Sciences*, *23* (6), 688 - 693. doi: 10.1175/1520-0469(1966)023⟨0688:TWDW⟩2.0.CO;2

Hasselmann, S., Hasselmann, K., Allender, J. H., & Barnett, T. P. (1985). Computations and Parameterizations of the Nonlinear Energy Transfer in a Gravity-Wave Specturm. Part II: Parameterizations of the Nonlinear Energy Transfer for Application in Wave Models. *J. Phys. Oceanogr.*, *15* (11), 1378-1391. doi: 10.1175/1520-0485(1985)015⟨1378:CAPOTN⟩2.0.CO;2

Hersbach, H., Bell, B., Berrisford, P., Biavati, G., Horányi, A., Muñoz Sabater, J., . . . Thépaut, J.-N. (2018a). ERA5 hourly data on pressure levels from 1979 to present. Copernicus Climate Change Service (C3S) Climate Data Store (CDS). *[Dataset]*. doi: https://doi.org/10.24381/cds.bd0915c6

Hersbach, H., Bell, B., Berrisford, P., Biavati, G., Horányi, A., Muñoz Sabater, J., . . . Thépaut, J.-N. (2018b). ERA5 hourly data on single levels from 1979 to present. Copernicus Climate Change Service (C3S) Climate Data Store (CDS). *[Dataset]*. doi: https://doi.org/10.24381/cds.adbb2d47

Hong, S.-Y., & Lim, J.-O. J. (2006). The WRF Single-Moment 6-Class Microphysics Scheme (WSM6). *Journal of the Korean Meteorological Society*, *42* , 129-151.

Iyer, S., Thomson, J., Thompson, E., & Drushka, K. (2022). Variations in wave slope and momentum flux from wave-current interactions in the tropical trade winds. *Journal of Geophysical Research: Oceans*, *127* (3), e2021JC018003. doi: https://doi.org/10.1029/2021JC018003

Janssen, P. A. E. M. (1989). Wave-induced stress and the drag of air flow over sea waves. *Journal of Physical Oceanography*, *19* (6), 745 - 754. doi: 10.1175/1520-0485(1989)019⟨0745:WISATD⟩2.0.CO;2

Janssen, P. A. E. M. (1991). Quasi-linear theory of wind-wave generation applied to wave forecasting. *J. Phys. Oceanogr.*, *21* (11), 1631-1642.

Jiang, H., & Chen, G. (2013). A Global View on the Swell and Wind Sea Climate by the Jason-1 Mission: A Revisit. *Journal of Atmospheric and Oceanic Technology*, *30* (8), 1833 - 1841. doi: 10.1175/JTECH-D-12-00180.1

Jiménez, P. A., Dudhia, J., González-Rouco, J. F., Navarro, J., Montávez, J. P., & García-Bustamante, E. (2012). A Revised Scheme for the WRF Surface Layer Formulation. *Monthly Weather Review*, *140* (3), 898 - 918. doi: 10.1175/MWR-D-11-00056.1

Kahma, K. K., Donelan, M. A., Drennan, W. M., & Terray, E. A. (2016). Evidence of Energy and Momentum Flux from Swell to Wind. *Journal of Physical Oceanography*, *46* (7), 2143 - 2156. doi: 10.1175/JPO-D-15-0213.1

Kantha, L. (2006). A note on the decay rate of swell. *Ocean Modelling*, *11* (1), 167-173. doi: https://doi.org/10.1016/j.ocemod.2004.12.003

Kudryavtsev, V., Chapron, B., & Makin, V. (2014). Impact of wind waves on the air-sea fluxes: A coupled model. *Journal of Geophysical Research: Oceans*, *119* (2), 1217-1236. doi: https://doi.org/10.1002/2013JC009412

Large, W. G., McWilliams, J. C., & Doney, S. C. (1994). Oceanic vertical mixing: A review and a model with a nonlocal boundary layer parameterization. *Reviews of Geophysics*, *32* (4), 363-403. doi: https://doi.org/10.1029/94RG01872

Lellouche, J.-M., Greiner, E., Le Galloudec, O., Garric, G., Regnier, C., Drevillon, M., . . . Le Traon, P.-Y. (2018). Recent updates to the Copernicus Marine Service global ocean monitoring and forecasting real-time 1/12° high-resolution system. *Ocean Science*, *14* (5), 1093–1126. doi: 10.5194/os-14-1093-2018

Liu, Q., Babanin, A., Fan, Y., Zieger, S., Guan, C., & Moon, I.-J. (2017). Numerical simulations of ocean surface waves under hurricane conditions: Assessment of existing model performance. *Ocean Modelling*, *118*, 73-93. doi: https://doi.org/10.1016/j.ocemod.2017.08.005

Liu, Q., Rogers, W. E., Babanin, A. V., Young, I. R., Romero, L., Zieger, S., ... Guan, C. (2019). Observation-based source terms in the third-generation wave model wavewatch iii: Updates and verification. *Journal of Physical Oceanography*, *49*(2), 489 - 517. doi: 10.1175/JPO-D-18-0137.1

Marshall, J., Ferrari, R., Forget, G., Maze, G., Andersson, A., Bates, N., ... Thomas, L. (2009). The Climode Field Campaign: Observing the Cycle of Convection and Restratification over the Gulf Stream. *Bulletin of the American Meteorological Society*, *90*(9), 1337 - 1350. doi: 10.1175/2009BAMS2706.1

Moon, I.-J., Hara, T., Ginis, I., Belcher, S. E., & Tolman, H. L. (2004). Effect of surface waves on air–sea momentum exchange. part i: Effect of mature and growing seas. *Journal of the Atmospheric Sciences*, *61*(19), 2321 - 2333. doi: 10.1175/1520-0469(2004)061⟨2321:EOSWOA⟩2.0.CO;2

Nakanishi, M., & Niino, H. (2004). An Improved Mellor–Yamada Level-3 Model with Condensation Physics: Its Design and Verification. *Boundary-Layer Meteorology*, *112*, 1-31. doi: 10.1023/B:BOUN.0000020164.04146.98

Nakanishi, M., & Niino, H. (2006). An Improved Mellor–Yamada Level-3 Model: Its Numerical Stability and Application to a Regional Prediction of Advection Fog. *Boundary-Layer Meteorology*, *119*, 397-407. doi: 10.1007/s10546-005-9030-8

Nakanishi, M., & Niino, H. (2009). Development of an improved turbulence closure model for the atmospheric boundary layer. *Journal of the Meteorological Society of Japan. Ser. II*, *87*(5), 895-912. doi: 10.2151/jmsj.87.895

Oost, W., Komen, G., Jacobs, C., & Van Oort, C. (2002). New evidence for a relation between wind stress and wave age from measurements during ASGAMAGE. *Boundary-Layer Meteorology volume*, *103*(3), 409 - 438. doi: 10.1023/A:1014913624535

Patton, E. G., Sullivan, P. P., Kosović, B., Dudhia, J., Mahrt, L., Žagar, M., & Marić, T. (2019). On the influence of swell propagation angle on surface drag. *Journal of Applied Meteorology and Climatology*, *58*(5), 1039 - 1059. doi: 10.1175/JAMC-D-18-0211.1

Phillips, O. M. (1985). Spectral and statistical properties of the equilibrium range in wind-generated gravity waves. *Journal of Fluid Mechanics*, *156*, 505–531. doi: 10.1017/S0022112085002221

Porchetta, S., Temel, O., Muñoz Esparza, D., Reuder, J., Monbaliu, J., van Beeck, J., & van Lipzig, N. (2019). A new roughness length parameterization accounting for wind–wave (mis)alignment. *Atmospheric Chemistry and Physics*, *19*(10), 6681–6700. doi: 10.5194/acp-19-6681-2019

Porchetta, S., Temel, O., Warner, J., Muñoz-Esparza, D., Monbaliu, J., van Beeck, J., & van Lipzig, N. (2021). Evaluation of a roughness length parametrization accounting for wind–wave alignment in a coupled atmosphere–wave model. *Quarterly Journal of the Royal Meteorological Society*, *147*(735), 825-846. doi: https://doi.org/10.1002/qj.3948

Quinn, P. K., Thompson, E. J., Coffman, D. J., Baidar, S., Bariteau, L., Bates, T. S., ... Zuidema, P. (2021). Measurements from the RV *Ronald H. Brown* and related platforms as part of the Atlantic Tradewind Ocean-Atmosphere Mesoscale Interaction Campaign (ATOMIC). *Earth System Science Data*, *13*(4), 1759–1790. doi: 10.5194/essd-13-1759-2021

Rascle, N., & Ardhuin, F. (2013). A global wave parameter database for geophysical applications. Part 2: Model validation with improved source term parameterization. *Ocean Modelling*, *70*, 174 - 188. (Ocean Surface Waves) doi:

10.1016/j.ocemod.2012.12.001

Rascle, N., Ardhuin, F., Queffeulou, P., & Croizé-Fillon, D. (2008). A global wave parameter database for geophysical applications. part 1: Wave-current–turbulence interaction parameters for the open ocean based on traditional parameterizations. *Ocean Modelling*, *25*(3), 154-171. doi: https://doi.org/10.1016/j.ocemod.2008.07.006

Renault, L., McWilliams, J. C., & Penven, P. (2017). Modulation of the Agulhas Current Retroflection and Leakage by Oceanic Current Interaction with the Atmosphere in Coupled Simulations. *Journal of Physical Oceanography*, *47*(8), 2077 - 2100. doi: 10.1175/JPO-D-16-0168.1

Renault, L., Molemaker, M. J., Gula, J., Masson, S., & McWilliams, J. C. (2016). Control and Stabilization of the Gulf Stream by Oceanic Current Interaction with the Atmosphere. *Journal of Physical Oceanography*, *46*(11), 3439 - 3453. doi: 10.1175/JPO-D-16-0115.1

Rieder, K. F., Smith, J. A., & Weller, R. A. (1994). Observed directional characteristics of the wind, wind stress, and surface waves on the open ocean. *Journal of Geophysical Research: Oceans*, *99*(C11), 22589-22596. doi: https://doi.org/10.1029/94JC02215

Rogers, W. E., Babanin, A. V., & Wang, D. W. (2012). Observation-Consistent Input and Whitecapping Dissipation in a Model for Wind-Generated Surface Waves: Description and Simple Calculations. *Journal of Atmospheric and Oceanic Technology*, *29*(9), 1329 - 1346. doi: 10.1175/JTECH-D-11-00092.1

Sauvage, C., Lebeaupin Brossier, C., Bouin, M.-N., & Ducrocq, V. (2020). Characterization of the air–sea exchange mechanisms during a Mediterranean heavy precipitation event using realistic sea state modelling. *Atmos. Chem. Phys.*, *20*(3), 1675–1699. doi: 10.5194/acp-20-1675-2020

Semedo, A., Sušelj, K., Rutgersson, A., & Sterl, A. (2011). A Global View on the Wind Sea and Swell Climate and Variability from ERA-40. *Journal of Climate*, *24*(5), 1461 - 1479. doi: 10.1175/2010JCLI3718.1

Seo, H., Miller, A. J., & Roads, J. O. (2007). The Scripps Coupled Ocean–Atmosphere Regional (SCOAR) Model, with Applications in the Eastern Pacific Sector. *Journal of Climate*, *20*(3), 381–402. doi: 10.1175/jcli4016.1

Seo, H., Song, H., O'Neill, L. W., Mazloff, M. R., & Cornuelle, B. D. (2021). Impacts of Ocean Currents on the South Indian Ocean Extratropical Storm Track through the Relative Wind Effect. *Journal of Climate*, *34*(22), 9093 - 9113. doi: 10.1175/JCLI-D-21-0142.1

Seo, H., Subramanian, A. C., Song, H., & Chowdary, J. S. (2019). Coupled effects of ocean current on wind stress in the bay of bengal: Eddy energetics and upper ocean stratification. *Deep Sea Research Part II: Topical Studies in Oceanography*, *168*, 104617. (Atmosphere-Ocean Dynamics of Bay of Bengal - Volume I) doi: https://doi.org/10.1016/j.dsr2.2019.07.005

Shchepetkin, A. F., & McWilliams, J. C. (2005). The regional oceanic modeling system (ROMS): a split-explicit, free-surface, topography-following-coordinate oceanic model. *Ocean Modelling*, *9*(4), 347-404. doi: https://doi.org/10.1016/j.ocemod.2004.08.002

Shin, H. H., Hong, S.-Y., & Dudhia, J. (2012). Impacts of the Lowest Model Level Height on the Performance of Planetary Boundary Layer Parameterizations. *Monthly Weather Review*, *140*(2), 664 - 682. doi: 10.1175/MWR-D-11-00027.1

Skamarock, W. C., Klemp, J. B., Dudhia, J., Gill, D. O., Barker, D., Duda, M. G., & Powers, J. G. (2008). A Description of the Advanced Research WRF Version 3. (NCAR/TN-475+STR). doi: 10.5065/D68S4MVH

Smedman, A., Högström, U., Sahleé, E., Drennan, W. M., Kahma, K. K., Pettersson, H., & Zhang, F. (2009). Observational Study of Marine Atmospheric

Boundary Layer Characteristics during Swell. *Journal of the Atmospheric Sciences*, *66*(9), 2747 - 2763. doi: 10.1175/2009JAS2952.1

Stevens, B., Bony, S., Farrell, D., Ament, F., Blyth, A., Fairall, C., … Zöger, M. (2021). EUREC^{4}A. *Earth System Science Data*, *13*(8), 4067–4119. doi: 10.5194/essd-13-4067-2021

Sullivan, P. P., Edson, J. B., Hristov, T., & McWilliams, J. C. (2008). Large-eddy simulations and observations of atmospheric marine boundary layers above nonequilibrium surface waves. *Journal of the Atmospheric Sciences*, *65*(4), 1225 - 1245. doi: 10.1175/2007JAS2427.1

Taylor, P. K., & Yelland, M. J. (2001, 02). The Dependence of Sea Surface Roughness on the Height and Steepness of the Waves. *Journal of Physical Oceanography*, *31*(2), 572-590. doi: 10.1175/1520-0485(2001)031⟨0572:TDOSSR⟩2.0.CO;2

The WAVEWATCH III Development Group. (2016). *User manual and system documentation of WAVEWATCH III version 5.16* (Tech. Rep. No. 329). College Park, MD, USA: NOAA/NWS/NCEP/MMAB. Retrieved from `https://polar.ncep.noaa.gov/waves/wavewatch/manual.v5.16.pdf`

Thompson, E., Fairall, C., Pezoa, S., & Bariteau, L. (2021). ATOMIC ship navigation, meteorology, seawater, fluxes: Near-surface meteorology, air-sea fluxes, surface ocean waves, and near surface ocean parameters (temperature, salinity, currents) and primary dataset of ship location and navigation estimated from in-situ and remote sensing instruments aboard NOAA Ship Ronald H. Brown in the North Atlantic Ocean, near Barbados: Atlantic Tradewind Ocean-Atmosphere Mesoscale Interaction Campaign 2020-01-09 to 2020-02-12 (NCEI Accession 0225427). *NOAA National Centers for Environmental Information. Dataset*. (Accessed 23 December 2021) doi: https://doi.org/10.25921/etxb-ht19

Thomson, J. (2012). Wave Breaking Dissipation Observed with “SWIFT” Drifters. *Journal of Atmospheric and Oceanic Technology*, *29*(12), 1866 - 1882. doi: 10.1175/JTECH-D-12-00018.1

Thomson, J., Moulton, M., de Klerk, A., Talbert, J., Guerra, M., Kastner, S., … Nylund, S. (2019). A new version of the SWIFT platform for waves, currents, and turbulence in the ocean surface layer. In *2019 IEEE/OES Twelfth Current, Waves and Turbulence Measurement (CWTM)* (p. 1-7). doi: 10.1109/CWTM43797.2019.8955299

Thomson, J., Thompson, E., Iyer, S., Drushka, K., & de Klerk, A. (2021). ATOMIC SWIFT drifters: Near-surface meteorology, air-sea fluxes, surface ocean waves, and near-surface ocean properties (turbulent dissipation rate, currents, temperature, salinity) estimated from in-situ and remote sensing instruments aboard six SWIFT drifters (Surface Wave Instrument Float with Tracking) launched and recovered for two different deployments from NOAA Ship Ronald H. Brown in the North Atlantic Ocean, near Barbados: Atlantic Tradewind Ocean-Atmosphere Mesoscale Interaction Campaign 2020-01-14 to 2020-02-11 (NCEI Accession 0225279). *NOAA National Centers for Environmental Information. Dataset*. (Accessed 23 December 2021) doi: https://doi.org/10.25921/s5d7-tc07

Tolman, H. L., Balasubramaniyan, B., Burroughs, L. D., Chalikov, D. V., Chao, Y. Y., Chen, H. S., & Gerald, V. M. (2002). Development and Implementation of Wind-Generated Ocean Surface Wave Modelsat NCEP. *Weather and Forecasting*, *17*(2), 311 - 333. doi: 10.1175/1520-0434(2002)017⟨0311:DAIOWG⟩2.0.CO;2

Villas Bôas, A. B., & Young, W. R. (2020). Directional diffusion of surface gravity wave action by ocean macroturbulence. *Journal of Fluid Mechanics*, *890*, R3. doi: 10.1017/jfm.2020.116

Wunsch, C. (1998). The Work Done by the Wind on the Oceanic General Circulation. *Journal of Physical Oceanography*, *28*(11), 2332 - 2340. doi: 10.1175/1520-0485(1998)028⟨2332:TWDBTW⟩2.0.CO;2

Zheng, Y., Alapaty, K., Herwehe, J. A., Genio, A. D. D., & Niyogi, D. (2016). Improving High-Resolution Weather Forecasts Using the Weather Research and Forecasting (WRF) Model with an Updated Kain–Fritsch Scheme. *Monthly Weather Review*, *144*(3), 833 - 860. doi: 10.1175/MWR-D-15-0005.1

Zou, Z., Song, J., Li, P., Huang, J., Zhang, J. A., Wan, Z., & Li, S. (2019). Effects of swell waves on atmospheric boundary layer turbulence: A low wind field study. *Journal of Geophysical Research: Oceans*, *124*(8), 5671-5685. doi: https://doi.org/10.1029/2019JC015153